

Internal gravity waves in stratified flows with and without vortical modes

Vincent Labarre,^{1,*} Pierre Augier,^{2,†} Giorgio Krstulovic,^{1,‡} and Sergey Nazarenko^{3,§}

¹*Université Côte d'Azur, Observatoire de la Côte d'Azur, CNRS, Laboratoire Lagrange, Nice, France*

²*Laboratoire des Écoulements Géophysiques et Industriels,*

Université Grenoble Alpes, CNRS, Grenoble-INP, F-38000 Grenoble, France

³*Université Côte d'Azur, CNRS, Institut de Physique de Nice - INPHYNI, Nice, France*

The comprehension of stratified flows is important for geophysical and astrophysical applications. The Weak Wave Turbulence theory aims to provide a statistical description of internal gravity waves propagating in the bulk of such flows. However, internal gravity waves are usually perturbed by other structures present in stratified flow, namely the shear modes and the vortical modes. In order to check whether a weak internal gravity wave turbulence regime can occur, we perform direct numerical simulations of stratified turbulence without shear modes, and with or without vortical modes at various Froude and buoyancy Reynolds numbers. We observe that removing vortical modes naturally helps to have a better overall balance between poloidal kinetic energy, involved in internal gravity waves, and potential energy. However, conversion between kinetic energy and potential energy does not necessarily show fluctuations around zero in our simulations, as we would expect for a system of weak waves. A spatiotemporal analysis reveals that removing vortical modes helps to concentrate the energy around the wave frequency, but it is not enough to observe a weak wave turbulence regime. Yet, we observe that internal gravity waves whose frequency are large compared to the eddy turnover time are present, and we also find evidences for slow internal gravity waves interacting by Triadic Resonance Instabilities in our strongly stratified flows simulations. Finally, we propose conditions that should be fulfilled in order to observe a weak internal gravity waves turbulence regime in real flows.

I. INTRODUCTION

As eddies in classical hydrodynamic turbulence, waves in nonlinear systems interact and transfer conserved quantities along scales in a cascade process. The Weak-Wave Turbulence (WWT) theory aims to provide a statistical description of the system when the nonlinearity is small [1–3]. The applications of this theory encompass capillary-gravity waves [4], gravito-inertial waves in rotating and stratified fluids [5–7], 2D acoustic waves [8], elastic plates [9], Alfvén waves in magnetohydrodynamics (MHD) [10], Kelvin waves in superfluids [11], density waves in Bose-Einstein condensates [12], and gravitational waves [13].

Three key hypotheses are used in weak-wave turbulence (WWT) theory. The first one is weak nonlinearity of the dynamical equations. This condition is often translated in terms of spatial scale separation: the considered scale on one side and the saturation scale on the other. The saturation scale is here defined as the scale at which the weak nonlinearity no longer holds, inducing wave breaking. This hypothesis is quite similar to the separation between the integral scale and the dissipative scale in the classical picture of 3D hydrodynamic turbulence, which is necessary for observing an inertial range. The second hypothesis corresponds to a separation of time scales. It requires that the linear time, given by the wave period τ_L , is much shorter than the nonlinear time of interactions between waves τ_{NL} [2]. The third hypothesis is that the nonlinear broadening $\delta\omega \sim 1/\tau_{NL}$, which measures the frequency of nonlinear interactions, must be larger than the frequency gap between wave modes $\Delta\omega$ in the discrete Fourier space. This last condition is necessary to permit enough nonlinear interactions among waves such that we can consider Fourier space as being continuous [14].

For many physical situations, at least one of the three hypotheses of WWT is broken in some range of scales, which reduces the validity of the theory [14, 15]. Yet, when scale separation is observed in space and time, a WWT range can emerge in wave energy spectra. Besides the practical difficulties for obtaining scale separation, testing WWT in isotropic systems is conceptually simpler. For this reason, main progress have been made in the experimental and numerical verification of WWT for elastic plates [16, 17], capillary-gravity waves [4, 18], density waves in Bose-Einstein condensates [19], and 2D acoustic waves [8].

* vincent.labarre@oca.eu

† pierre.augier@univ-grenoble-alpes.fr

‡ giorgio.krstulovic@oca.eu

§ sergey.nazarenko@unice.fr

Anisotropic turbulence is, generally speaking, more difficult to investigate than isotropic turbulence because of the reduced number of symmetries of the considered system. For example, it has been shown that studying 2D spatial spectra instead of 1D integrated spectra is essential to investigate stratified turbulence [20]. Anisotropy makes the problem multidimensional in Fourier space, which makes the notion of spectral energy fluxes, and other relevant quantities, more difficult to define and calculate than in isotropic turbulence [21]. An additional difficulty is that scale separations required by WWT can also be anisotropic. For linearly stratified flows, the weak nonlinearity of the Navier-Stokes equations requires that the spatial scale separation

$$k/k_b \ll 1 \quad (1)$$

is satisfied, where $k_b = N/U_h$ is the buoyancy wave-vector, k is the wave-vector modulus, U_h is the rms of the horizontal velocity, and N is the Brunt-Väisälä frequency. This condition should be fulfilled in order to avoid wave-breaking [22]. The temporal scale separation between linear waves and eddies leads to the different condition

$$\tau_L/\tau_{NL} = \frac{(\varepsilon_K k^2)^{1/3}}{N k_h/k} \ll 1, \quad (2)$$

where ε_K is the kinetic energy dissipation rate, k_h is the horizontal wave-vector modulus, $\tau_L = 2\pi k/(N k_h)$ is the period of internal gravity waves, and $\tau_{NL} = 2\pi/(k^2 \varepsilon_K)^{1/3}$ is the eddy turnover time [20]. Physically, when $\tau_L/\tau_{NL} \ll 1$, the waves are faster than the typical time of their nonlinear interactions. Due to the anisotropic dispersion relation of internal gravity waves, time scale separation is less valid for small k_h , and even impossible for modes with $k_h = 0$. Consequently, separation of time scales can be violated even if a large separation of spatial scales is observed (i.e. $k/k_b \ll 1$). A similar situation takes place in plasmas under the effect of a strong magnetic field, or strongly rotating and stratified flows. It is therefore more difficult to observe signatures of WWT in anisotropic systems.

Stratified turbulence is not only an interesting conceptual problem, but it is also essential for understanding geophysical flows. [23, 24]. In particular, sub-grid parameterizations in climate models require an understanding of the role of waves in mixing [25, 26]. It is therefore not surprising that stratified turbulence received a particular attention from both the “strong” turbulence community [22, 27–36], and the WWT community [5, 11, 37–39]. It turns out that internal waves are effectively important in the dynamics and mixing in stratified flows [40–42], and that three-wave resonant interactions are responsible for slow energy transfers between different scales [43–45]. Internal waves can be excited, for example, by tides [46] or by linearly unstable wave attractors [43]. However, many questions and issues remain about the applicability of WWT to stratified flows. In particular, it is not yet clear under which conditions a weak wave turbulence regime could occur.

It has been showed that a wave dominated region should lie in the spectral region defined by $\tau_L/\tau_{NL} < 1/3$ [20], in agreement with observations made for MHD [47]. However, the observation of a system of weakly interacting internal gravity waves is still delicate due to non-wave structures such as shear modes (purely vertical shear) and vortical modes (vertical vorticity). The same problem arises in rotating flows, in which the geostrophic modes play the role of the non-propagative structures. It has been ingeniously shown that tidal forcing is very efficient at triggering weakly nonlinear internal gravity waves [46], in a way reminiscent of the inertial waves’ excitation by libration in rotating fluids [48, 49]. Experimentalists overcame this difficulty by using honeycomb grids at the top and bottom boundaries of a rotating tank to dissipate geostrophic modes efficiently, allowing them to observe weak inertial wave turbulence [50, 51], in a similar fashion to the numerical study of [48]. More recently, it has been observed that resonance with the container modes also prevent to observe weak internal gravity wave turbulence, and that the introduction of slightly tilted panels at the top and at the bottom of the fluid domain allows to inhibit the emergence of these modes [52]. All these works point out that some wave systems can generate non-wave motions that can severely affect the wave dynamics and should be suppressed in experiments aiming to observe wave turbulence. In stratified flows these modes correspond to vertical shear, vertical vorticity, an eventually the container modes.

The most commonly used prediction of WWT is the scale-invariant stationary solution to the kinetic equation. This solution gives the expected spatial energy spectra of waves in the statistically steady state. There are two types of solutions: the thermodynamic equilibrium solution (Rayleigh-Jeans spectra), and the non-equilibrium solutions that are linked to the cascade of the dynamical invariants of the system along scales (Kolmogorov-Zakharov spectra) [2]. It is important to note that the Kolmogorov-Zakharov spectra are obtained after the Zakharov transformation, which can add spurious solutions. Therefore, these spectra can be considered as valid only if the collision integral in the original wave kinetic equation converges. The importance of the nonlinear interactions among internal gravity waves was recognized early, leading to several derivations of waves kinetic equations (see [53, 54]). Derivation of the Kolmogorov-Zakharov spectra in the limit of large vertical wave-numbers $k_z \simeq k \gg k_h$ can be found in [5, 37]. This

candidate solution corresponds to an energy cascade, and is given by the energy spectra

$$E(k_h, k_z) \sim k_h^{-3/2} k_z^{-3/2} \quad \text{and} \quad E(\omega, k_z) \sim \omega^{-3/2} k_z^{-2}, \quad (3)$$

where the change of coordinates is defined by the dispersion relation $E(\omega, k_z) = E(k_h, k_z) (\partial\omega_{\mathbf{k}}/\partial k_h)^{-1}$. Yet, it was noted that this candidate does not satisfy the requirement of locality, i.e. the collision integral diverges on it. In the other words, it is not a valid mathematical solution of the kinetic equation. Later, it was shown that power law solutions $E(k_h, k_z) \sim k_h^{-\alpha_h} k_z^{-\alpha_z}$ have convergent collision integral's contributions only on the segment $\alpha_h \in]2, 3[, \alpha_z = 1$ [38, 55]. The collision integral was then computed numerically on this segment, and it was deduced that the only scale invariant stationary solution to the kinetic equation was close to

$$E(k_h, k_z) \sim k_h^{-1.69} k_z^{-1} \quad \text{and} \quad E(\omega, k_z) \sim \omega^{-1.69} k_z^{-1.69}. \quad (4)$$

It was also shown that the dominant contributions to the collision integral corresponds to non-local transfers first identified by McComas [56], notably the Parametric Subharmonic Instability (PSI) [53, 56] observed in oceans [57] and experiments [45], consisting in the resonant interaction of a primary wave and two smaller-scale waves of nearly half the frequency.

When $k/k_b \gg 1$, nonlinearity is not small and WWT is not valid. Based on the idea that there exists a range of spatial scales where buoyancy force has the same order of magnitude than inertia, the following 1D integrated energy spectra

$$E_{1D}(k_h) \sim \varepsilon_\kappa^{2/3} k_h^{-5/3} \quad \text{and} \quad E_{1D}(k_z) \sim N^2 k_z^{-3} \quad (5)$$

where predicted [30]. In the strong wave turbulence context, these predictions can also be obtained using critical balance arguments [2, 58]. At even smaller scales, where stratification is negligible, an isotropic range with the energy spectra

$$E_{1D}(k) \sim \varepsilon_\kappa^{2/3} k^{-5/3} \quad (6)$$

is expected. It happens when $k_b < k_O \ll k \ll k_\eta$ where k_O is the Ozmidov wave-vector and k_η is the Kolmogorov wave-vector.

The present study first deals with the existence and properties of a weak internal gravity wave turbulence regime. To this end, we perform numerical simulations of stratified turbulence at various Brunt-Väisälä frequency and viscosity. In the same spirit as simulations and experiments of rotating flows [48, 50, 51], we remove shear modes in all of our simulations. For each values of the control parameters, we perform two “twin” simulations: one where the vortical modes remain, and one where vortical modes are removed from the dynamics by a projection in spectral space [59]. It is worth noting that numerical simulations of reduced dynamical equations (i.e., without non-wave structures) of stratified rotating flows in the hydrostatic balance have already been conducted to remove non-wave structures [60]. Despite the simplifications, these simulations reproduced some key features of oceanic internal-wave spectra, such as the accumulation of energy at near-inertial waves and realistic frequency and horizontal wave-number dependencies of spatiotemporal spectra. In the present work, we do not account for rotation. However, our simulations allows to investigate the role of vortical modes on the dynamics of stratified flows outside the hydrostatic balance approximation. The manuscript is organized as follows. In section II, we present our methodology including a presentation of the code and the simulations. Our results are presented in section III. Subsection III A is devoted to the study of flow regimes in the control parameter space. It shows, as expected, that WWT is naturally more likely to occur at high stratification and without vortical modes. Subsections III B and III C deal with the spatiotemporal analysis of a couple of strongly stratified simulations to investigate further the presence of linear waves in spatial scales. In the last subsection III D, we propose a simple diagnostic to evaluate the predominance of waves in the parameter space. We give concluding remarks in section IV.

II. METHODS

We use the 3D Navier-Stokes equations under the Boussinesq approximation:

$$\nabla \cdot \mathbf{v} = 0 \quad (7)$$

$$\partial_t \mathbf{v} + \mathbf{v} \cdot \nabla \mathbf{v} = b \mathbf{e}_z - \nabla p + \nu \nabla^2 \mathbf{v} + \mathbf{f}, \quad (8)$$

$$\partial_t b + \mathbf{v} \cdot \nabla b = -N^2 v_z + \kappa \nabla^2 b, \quad (9)$$

where (x, y, z) will represent the three spatial coordinates in the cartesian frame $(O, \mathbf{e}_x, \mathbf{e}_y, \mathbf{e}_z)$, \mathbf{e}_z is the stratification axis, $\mathbf{v} = (v_x, v_y, v_z)$ is the velocity, b the buoyancy, p the total kinematic pressure, N the Brunt-Väisälä frequency, ν the viscosity, κ the diffusivity and \mathbf{f} is the velocity forcing. The buoyancy is defined as $b = -g\rho'/\rho_0$, where g is the acceleration due to gravity, ρ_0 is the average density of the fluid at $z = 0$, and ρ' is the density perturbation with respect to the average linear density profile $\bar{\rho}(z) = \rho_0 + (d\bar{\rho}/dz)z$. The Schmidt number $Sc = \nu/\kappa$ is fixed to one.

We simulate forced-dissipated flows with the pseudo-spectral solver `ns3d.strat` from the FluidSim software [61] (an open-source Python package of the FluidDyn project [62] using Fluidfft [63] to compute the Fast Fourier Transforms). The forcing, which will be described in details at the end of this section and in Appendix A, is computed in spectral space such that the kinetic energy injection rate P_K is constant and equal to unity. The physical input parameters are the Brunt-Väisälä frequency N and the diffusive coefficients $\nu = \kappa$, but in practice, we identify our simulations with the couple (N, \mathcal{R}_i) , where $\mathcal{R}_i \equiv P_K/(\nu N^2)$ is the input buoyancy Reynolds number. The turbulent non-dimensional numbers characterizing the statistically stationary flow are the horizontal turbulent Froude number and the buoyancy Reynolds number [31] that are respectively

$$F_h = \frac{\varepsilon_\kappa}{U_h^2 N} \quad \text{and} \quad \mathcal{R} = \frac{\varepsilon_\kappa}{\nu N^2}, \quad (10)$$

where ε_κ is the kinetic energy dissipation rate and U_h the rms of the horizontal velocity. Note that the turbulent Reynolds number is given by $Re = \mathcal{R}/F_h^2$. We also compute the buoyancy and the Ozmidov wave-vectors $k_b \equiv N/U_h$ and $k_O \equiv \sqrt{N^3/P_K}$. All the quantities presented in this manuscript are computed from averaging when stationarity is reached. A list of the simulations, with relevant parameters and physical quantities, is given in Appendix I.

In this study, we consider a periodic domain of horizontal size $L_x = L_y = L_h = 3$ and vertical size L_z . We note (n_x, n_y, n_z) the numbers of collocation points in the three spatial directions, with $n_x = n_y \equiv n_h$. We chose n_z in order to have an isotropic mesh in physical space, i.e. $L_z/n_z = L_h/n_h$. We decrease L_z with N . Typically, $L_z \propto 1/N$, while L_h is kept constant for all simulations. More precisely, the aspect ratio L_z/L_h is 1/2 for $N \leq 20$, 1/4 for $N \leq 60$, and 1/8 for $N \geq 80$. This choice is motivated by the fact that the unforced and undissipated Boussinesq equations are self-similar in the limit $F_h \rightarrow 0$, with similarity variable zN/U , where U is the typical velocity [27]. In that way, we simulate few layers (of height $L_b = U/N$) for all our simulations.

To reduce the computational costs, we first simulate the transient state with a coarse resolution with $n_h = 320$. For these simulations, two hyperdiffusive terms $-\nu_4 \nabla^4 \mathbf{v}$ and $-\kappa_4 \nabla^4 b$ are added to (8) and (9), respectively, in order to keep the dissipative range in the simulated scales and avoid thermalisation at small scales. Once a statistically steady-state is reached, we increase the resolution of the simulation while decreasing hyper-viscosity. Then the simulation is run until reaching a new statistically steady state. The previous step is repeated until reaching the highest resolution. We measure the turbulent kinetic dissipation rates ε_{κ_2} and ε_{κ_4} based on both viscosities, and the total kinetic energy dissipation rate $\varepsilon_\kappa = \varepsilon_{\kappa_2} + \varepsilon_{\kappa_4}$. The product of the maximal wave-vector k_{\max} with the Kolmogorov scale $\eta \equiv (\nu^3/\varepsilon_\kappa)^{1/4}$ is computed to quantify how close our simulations are from true Direct Numerical Simulations (DNS). In practice, it is common to consider that simulations are proper DNS with well-resolved small scales when $k_{\max}\eta > 1$ [31, 64]. For the statistically stationary state, the time average of the total energy dissipation rate is equal to the injection rate P_K so that the product $k_{\max}\eta$ depends mostly on ν and n_h . For most couples (N, \mathcal{R}_i) , the resolution of the larger simulation is fine enough ($k_{\max}\eta \gtrsim 1$) so that the hyperdiffusion is zero or negligible. For example, the two simulations analyzed in details in the next section (Figures 4 to 15) are proper DNS with $k_{\max}\eta$ equal to 0.99 and 1.05, respectively (see table I). There are also few simulations with $0.45 < k_{\max}\eta < 1$ (19 out of 78 simulations), which remain slightly under-resolved and affected by hyper-viscosity. In that case, small-scales and flow statistics should be analyzed carefully. We checked that these simulations do not change the results presented here. The Fourier transform of the velocity field $\hat{\mathbf{v}} = (\hat{v}_x, \hat{v}_y, \hat{v}_z)$ can be written using the poloidal-toroidal-shear decomposition (see e.g. [32, 36, 59, 65–67])

$$\hat{\mathbf{v}} = \begin{cases} \hat{v}_p \mathbf{e}_{p\mathbf{k}} + \hat{v}_t \mathbf{e}_{t\mathbf{k}} & \text{if } k_h \neq 0, \\ \hat{\mathbf{v}}_s = \hat{v}_x \mathbf{e}_x + \hat{v}_y \mathbf{e}_y & \text{if } k_h = 0, \end{cases} \quad (11)$$

where

$$\mathbf{e}_{\mathbf{k}} = \frac{\mathbf{k}}{k}, \quad \mathbf{e}_{p\mathbf{k}} = \frac{\mathbf{k} \times (\mathbf{k} \times \mathbf{e}_z)}{|\mathbf{k} \times (\mathbf{k} \times \mathbf{e}_z)|}, \quad \mathbf{e}_{t\mathbf{k}} = \frac{\mathbf{e}_z \times \mathbf{k}}{|\mathbf{e}_z \times \mathbf{k}|}. \quad (12)$$

\hat{v}_p is the poloidal component, \hat{v}_t the toroidal component, $\hat{\mathbf{v}}_s$ the shear modes component, $\mathbf{k} = (k_x, k_y, k_z)$ denotes the wave-vector, $k = |\mathbf{k}| = \sqrt{k_x^2 + k_y^2 + k_z^2}$ is its modulus, and $k_h = \sqrt{k_x^2 + k_y^2}$ is the modulus of the horizontal

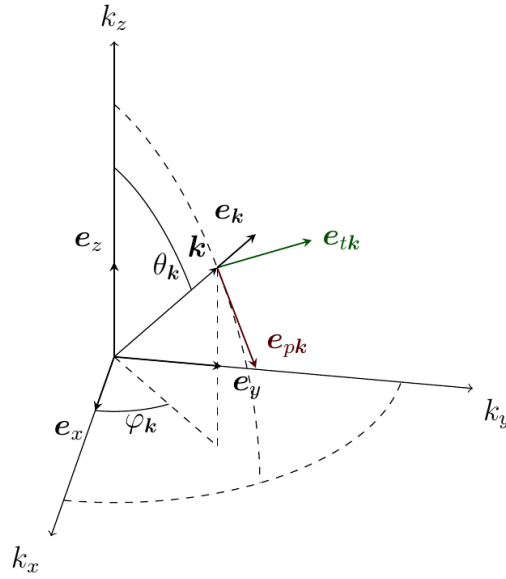


FIG. 1. Illustration of the poloidal-toroidal basis ($\mathbf{e}_k, \mathbf{e}_{pk}, \mathbf{e}_{tk}$) defined by equations (12). θ_k is the angle between \mathbf{e}_z and \mathbf{e}_k . φ_k is the angle between the horizontal projection of \mathbf{k} and \mathbf{e}_x .

component of the wave-vector (Figure 1). Since the toroidal component \hat{v}_t corresponds only to the vertical vorticity ($\hat{\Omega}_z = ik\hat{v}_t \sin \theta_k$, with $\boldsymbol{\Omega} = \nabla \times \mathbf{v}$ being the vorticity), we also denote it as the ‘‘vortical’’ velocity.

In spectral space, once projected, the equations of motion (7-9) read

$$\begin{cases} \dot{\hat{v}}_p &= -(\widehat{\mathbf{v} \cdot \nabla \mathbf{v}}) \cdot \mathbf{e}_{pk} - \hat{b} \sin \theta_k - \nu k^2 \hat{v}_p + \hat{\mathbf{f}} \cdot \mathbf{e}_{pk} \\ \dot{\hat{v}}_t &= -(\widehat{\mathbf{v} \cdot \nabla \mathbf{v}}) \cdot \mathbf{e}_{tk} - \nu k^2 \hat{v}_t + \hat{\mathbf{f}} \cdot \mathbf{e}_{tk} \\ \dot{\hat{b}} &= -\widehat{\mathbf{v} \cdot \nabla b} + N^2 \hat{v}_p \sin \theta_k - \kappa k^2 \hat{b} \end{cases} \quad \text{for } k_h \neq 0 \quad (13)$$

and

$$\begin{cases} \dot{\hat{v}}_s &= -\widehat{\mathbf{v} \cdot \nabla \mathbf{v}_h} - \nu k^2 \hat{v}_s, \\ \dot{\hat{b}} &= -\widehat{\mathbf{v} \cdot \nabla b} - \kappa k^2 \hat{b} \end{cases} \quad \text{for } k_h = 0, \quad (14)$$

where $\mathbf{v}_h = (v_x, v_y, 0)$ is the horizontal velocity and $\widehat{\cdot}$ denotes the Fourier transform. We will also note $k_i \in \Delta k_i \mathbb{Z}$ with $\Delta k_i = 2\pi/L_i$ for $i = x, y, z$, and hereafter assume $\Delta k_x = \Delta k_y \equiv \Delta k_h$. Without forcing and dissipation, the linearized equations (13-14) can be written as

$$\hat{a} = -i\omega_k \hat{a}, \quad \hat{a}^{(0)} = 0, \quad \text{if } k_h \neq 0 \quad (15)$$

$$\hat{v}_s = \mathbf{0}, \quad \hat{b} = 0 \quad \text{if } k_h = 0, \quad (16)$$

where

$$\hat{a} = \frac{\hat{v}_p - i\frac{\hat{b}}{N}}{\sqrt{2\omega_k}}, \quad \text{and} \quad \omega_k = N \frac{k_h}{k} = N \sin \theta_k \quad (17)$$

are the waves modes and the pulsation of the waves, θ_k is the angle between \mathbf{k} and the stratification axis \mathbf{e}_z , and $\hat{a}^{(0)} \propto \hat{v}_t$ are the vortical modes. Equations (15-16) show that both shear modes and vortical modes have zero frequency. This means that linear waves can only exist in the poloidal velocity and the buoyancy, but not in the toroidal velocity nor the shear velocity.

We are motivated by forcing internal gravity waves, which only involve the poloidal part of the velocity field and have an anisotropic dispersion relation. Therefore, we use an anisotropic, poloidal velocity forcing $\hat{\mathbf{f}} = \hat{f} \mathbf{e}_{pk}$. The flow is forced at large spatial scales $\{\mathbf{k} \mid 5 \leq k/\Delta k_h \leq 20\}$ and small angle $\{\mathbf{k} \mid |\omega_k/N - \sin \theta_f| \leq 0.05\}$ where $\sin \theta_f = 0.3$,

meaning that relatively slow internal waves are forced. The forcing scheme is described in Appendix A. It is neither harmonic nor given by a stochastic differential equation. Instead, a time correlated forcing is computed via generations of pseudo random numbers and time interpolations. Its correlation time is equal to the period of the forced waves $T_c = 2\pi/(N \sin \theta_f)$. The forcing is normalized such that the kinetic injection rate P_K is always equal to 1. Forcing slow waves is motivated by oceanic applications, where waves are generated, among other processes, by slow tides [25, 68]. Low frequency forcing is also used in order to have a scale separation between forced frequencies and the Brunt-Väisälä frequency so that one can potentially reproduce features of the oceanic temporal spectra close to N .

The time advancement is performed using the 4th order Runge-Kutta scheme. All modes with wave-number modulus larger than $k_{\max} = 0.8(n_h/2)\Delta k_h$ are truncated to limit aliasing. We checked that this 0.8 spherical truncation is a good compromise consistent with our other numerical choices. Shear modes and vertically invariant vertical velocity (internal waves at $\omega = N$), which are absent in flows bounded by walls, are also removed in our simulations by fixing nonlinear transfers to these modes to zero. For the simulations without vortical modes, the toroidal projection of the velocity and of the nonlinear transfers are set to zero. Smith and Waleffe [65] used a similar procedure in order to distangle the roles of potential vorticity modes and waves modes in rotating stratified turbulence.

Without dissipation and forcing, equations (7-9) conserve the total energy $E = \int [\mathbf{v}^2/2 + b^2/(2N^2)] dx dy dz$ and the potential vorticity $\Pi = \boldsymbol{\Omega} \cdot (N^2 \mathbf{e}_z + \nabla b)$ is a Lagrangian invariant [69]. It follows that the spatial average of any function of Π is conserved. As a special case, the potential enstrophy

$$V \equiv \frac{1}{2} \int \Pi^2 dx dy dz \quad (18)$$

$$= \frac{1}{2} \int N^4 \Omega_z^2 dx dy dz + \int N^2 \Omega_z \boldsymbol{\Omega} \cdot \nabla b dx dy dz + \frac{1}{2} \int (\boldsymbol{\Omega} \cdot \nabla b)^2 dx dy dz \quad (19)$$

$$\equiv V_2 + V_3 + V_4 \quad (20)$$

is an invariant of equations (7-9) in absence of dissipation and forcing. For a flow without vertical vorticity $V_2 = V_3 = 0$.

III. RESULTS

A. Regimes and global energy distribution

In this subsection, we study the anisotropy of the flow and global energy budget in the (F_h, \mathcal{R}) plane. To discuss stratified turbulence regimes, it is useful to introduce a large and a small scale isotropy coefficients [70]. The former is based on the kinetic energy components

$$I_{\text{kin}} = \frac{3E_{\text{kin},z}}{E_{\text{kin}}} \quad (21)$$

where $E_{\text{kin},z}$ is the vertical velocity energy and E_{kin} is the total kinetic energy. The small scale isotropy coefficient is computed using the kinetic energy dissipation rates, namely

$$I_{\text{diss}} = \frac{1 - \varepsilon_{\text{kin},z}/\varepsilon_{\text{kin}}}{(1 - 1/3)} \quad (22)$$

where $\varepsilon_{\text{kin},z}$ is the energy dissipation rate due to vertical gradients. Both I_{kin} and I_{diss} are equal to unity for an isotropic flow. Conversely, I_{kin} and I_{diss} should be close to zero if the flow is strongly anisotropic. When vortical modes are removed, we rather use

$$I_{\text{kin}} = \frac{2E_{\text{kin},z}}{E_{\text{kin}}} \quad (23)$$

because it is expected that only half of the kinetic energy is contained in the vertical velocity field. Figure 2 shows the variations of I_{kin} and I_{diss} with (F_h, \mathcal{R}) . Small points correspond to strong anisotropic energy dissipation, while large points correspond to isotropic energy dissipation. Dark points correspond to strong large-scale isotropy, while light points correspond to isotropic flows. The combination of I_{kin} and I_{diss} allows to distinguish between four regimes (Figure 2(a)): the passive scalar regime where $I_{\text{kin}} \simeq 1$, the weakly stratified regime where $0.5 \lesssim I_{\text{kin}} \lesssim 1$, and the strongly stratified regimes where $I_{\text{kin}} \leq 0.5$. As explained in [31], the strongly stratified flows fall in two regimes: The Layered Anisotropic Stratified Turbulence (LAST) regime where the dissipation is isotropic because a 3D turbulence

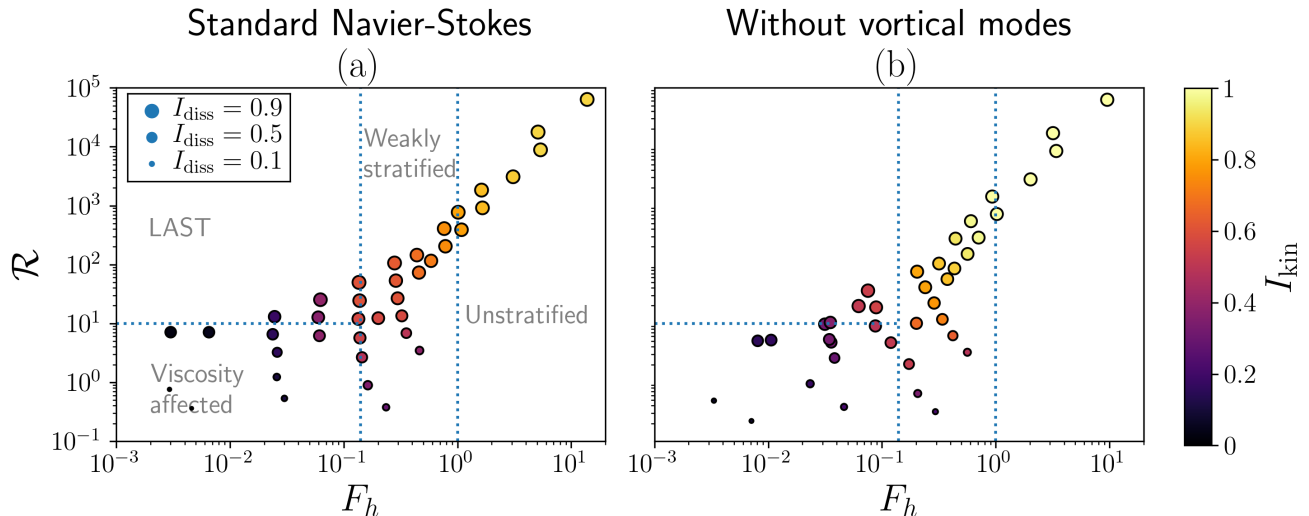


FIG. 2. Classification of regimes in our simulations using the isotropy coefficients. The large scale isotropy coefficient I_{kin} is given by the color-scale, and the small scale isotropy coefficient I_{diss} by the size of the symbols. For simulations with vortical modes (a), definitions (21-22) are used. For simulations without vortical modes (b), definitions (23) are used. The dotted blue lines correspond to $\mathcal{R} = 10$, $F_h = 0.14$, and $F_h = 1$.

range can develop, typically when $\mathcal{R} \geq 10$; The viscosity affected regime where the small dissipative scales remain affected by the anisotropy. WWT is foreseen at small F_h at some unknown values of \mathcal{R} . We observe that removing vortical modes does not modify this picture (Figure 2(b)). However, for a given (F_h, \mathcal{R}) , the isotropy coefficients tend to have bigger values when the vortical modes are removed.

We denote

$$E_{\text{pot}} = \frac{1}{2N^2} \sum_{\mathbf{k}} |\hat{b}|^2, \quad E_{\text{polo}} = \frac{1}{2} \sum_{\mathbf{k}} |\hat{v}_p|^2, \quad E_{\text{toro}} = \frac{1}{2} \sum_{\mathbf{k}} |\hat{v}_t|^2, \quad \tilde{\mathcal{D}} = \frac{E_{\text{polo}} - E_{\text{pot}}}{E_{\text{polo}} + E_{\text{pot}}} \quad (24)$$

which are, respectively, the potential energy, the poloidal kinetic energy, the vortical modes (toroidal) kinetic energy, and the relative difference between poloidal and potential energy. We also note $E = E_{\text{pot}} + E_{\text{polo}} + E_{\text{toro}}$ the total energy. Figure 3 shows the vortical modes energy ratio E_{toro}/E and $\tilde{\mathcal{D}}$ as a function of F_h and \mathcal{R} . For waves, we expect to observe an equipartition between the poloidal kinetic energy and potential energy. Consequently, both E_{toro}/E and $\tilde{\mathcal{D}}$ should be close to zero for a system mainly composed by internal gravity waves. We observe that vortical modes energy becomes dominant at high stratification (low F_h) if they are not removed from the dynamics in these simulations with $\mathcal{R} \geq 0.1$ (Figure 3 (a)). The ratio E_{toro}/E is the lowest at intermediate stratification $F_h \simeq 0.1 - 0.3$ and low values of \mathcal{R} . However, the same simulations are marked by a predominance of potential energy over poloidal energy, $\tilde{\mathcal{D}} < 0$ (Figure 3 (b)), meaning that these weakly stratified flows do contain other structures than waves. When vortical modes are removed, we can obtain flows with a global balance between poloidal and potential energies ($\tilde{\mathcal{D}} \simeq 0$) at high stratification. Consequently, a flow governed by weak nonlinear interactions between waves may be obtained at high stratification by removing vortical modes. In the two next subsections, we perform a spatiotemporal analysis of a couple of strongly stratified turbulent simulations with $(N, \mathcal{R}_i \equiv P_K/\nu N^2) = (40, 20)$ and aspect ratio $L_z/L_h = 1/4$. Figure 4 shows the buoyancy fields for these two simulations with the same color scale. We observe that the flow is layered in the vertical direction and that overturning (horizontal vorticity) is present with or without vortical modes. It is a standard feature of strongly stratified turbulence [22, 30, 31, 66]. With vortical modes, the vertical vorticity is not zero (Figure 4(a)) so the buoyancy has a different structure than when vortical modes are absent (Figure 4(b)). Without vortical modes the dynamics in the horizontal direction is irrotational and the buoyancy field has a larger amplitude.

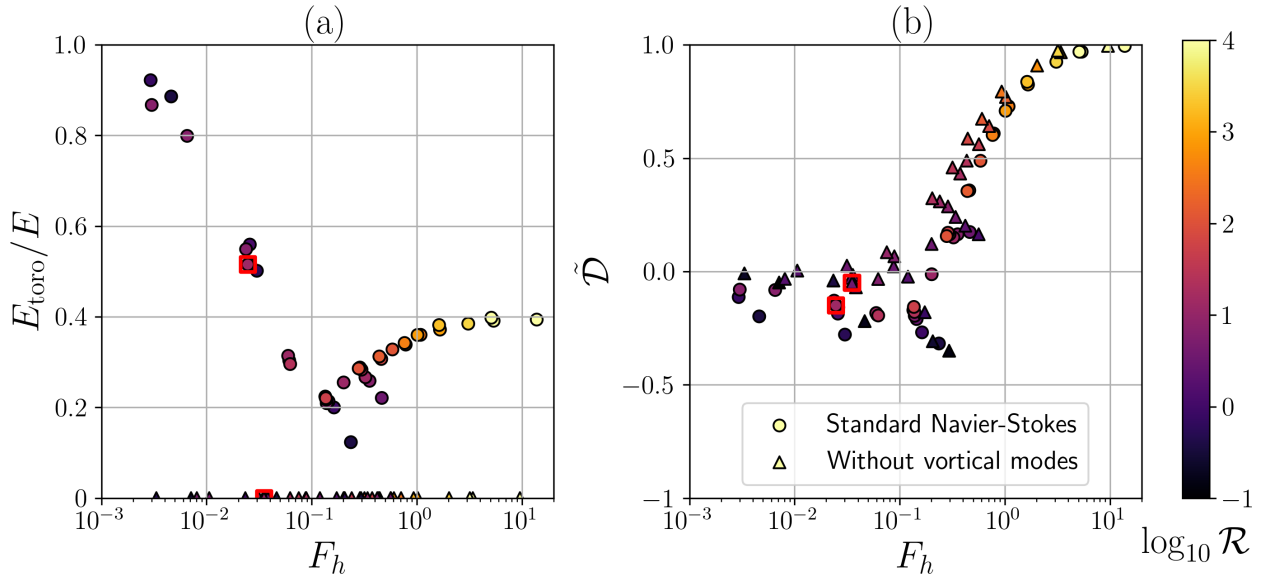


FIG. 3. Vortical modes to total energy ratio (a) and relative difference between poloidal and potential energies $\tilde{\mathcal{D}} = (E_{\text{polo}} - E_{\text{pot}})/(E_{\text{polo}} + E_{\text{pot}})$ (b) vs F_h for simulations with or without vortical modes. The red boxes indicate the simulations with $(N, \mathcal{R}_i) = (40, 20)$ investigated in the next subsections.

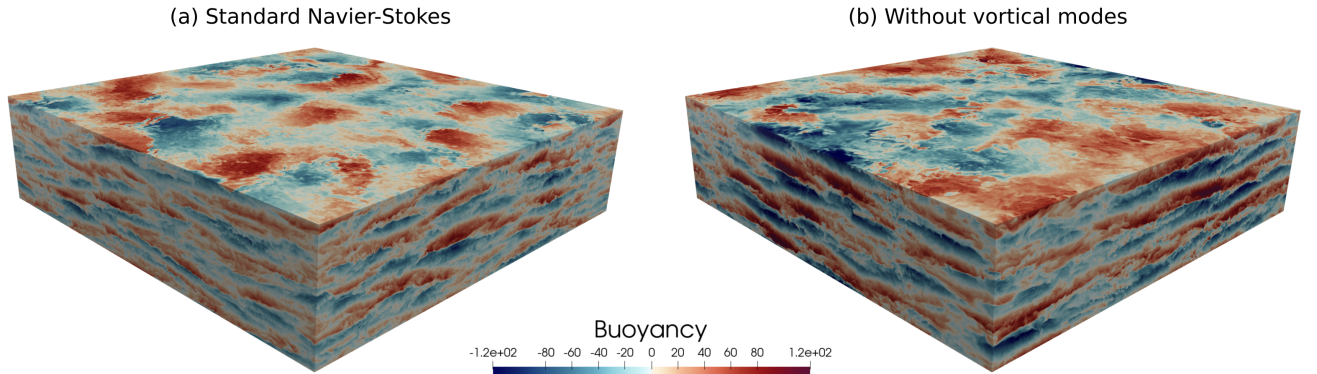


FIG. 4. Snapshots of the buoyancy fields for simulations $(N, \mathcal{R}_i) = (40, 20)$ with (a) and without (b) vortical modes.

B. Energy budget in the strongly stratified regime

It is expected that the spatial energy budget will depend on the ratio of temporal timescales. In particular the nonlinearity parameter used for several physical systems, including stratified and rotating turbulence [20, 58] and MHD [47, 71] is

$$\chi_{\mathbf{k}} \equiv \frac{\tau_L}{\tau_{\text{NL}}} = \frac{(\varepsilon_{\text{K}} k^2)^{1/3}}{N k_h / k} = \frac{k}{k_h} \left(\frac{k}{k_O} \right)^{2/3} = \frac{1}{\sin \theta_{\mathbf{k}}} \left(\frac{k}{k_O} \right)^{2/3}. \quad (25)$$

It represents the ratio between the period of the linear wave, $\tau_L = 2\pi k / (N k_h)$, and the eddy turnover time $\tau_{\text{NL}} = 2\pi / (\varepsilon_{\text{kin}} k^2)^{1/3}$ for a given wave-vector. In a similar way, we introduce the wave dissipation parameter

$$\gamma_{\mathbf{k}} \equiv \frac{\tau_L}{\tau_{\nu}} = \frac{\nu k^2}{N k_h / k} = \frac{k}{k_h} \left(\frac{k}{k_d} \right)^2 = \frac{1}{\sin \theta_{\mathbf{k}}} \left(\frac{k}{k_d} \right)^2 \quad (26)$$

which represents the ratio between the period of the linear wave and the dissipation time $\tau_\nu = 2\pi/(\nu k^2)$. In the last equation, we have introduced the wave dissipation wave-vector $k_d \equiv \sqrt{N/\nu}$. The kinetic energy and potential energy budgets for one Fourier mode read

$$\left\langle \frac{1}{2} \frac{d|\hat{\mathbf{v}}|^2}{dt} \right\rangle = \mathcal{I}_{\mathbf{k}} + \mathcal{T}_{\text{kin},\mathbf{k}} - \mathcal{B}_{\mathbf{k}} - \varepsilon_{\text{kin},\mathbf{k}}, \quad \text{and} \quad \left\langle \frac{1}{2N^2} \frac{d|\hat{b}|^2}{dt} \right\rangle = \mathcal{T}_{\text{pot},\mathbf{k}} + \mathcal{B}_{\mathbf{k}} - \varepsilon_{\text{pot},\mathbf{k}}, \quad (27)$$

where

$$\begin{aligned} \mathcal{I}_{\mathbf{k}} &= \left\langle \Re \left(\hat{\mathbf{f}} \cdot \hat{\mathbf{v}}^* \right) \right\rangle, & \mathcal{T}_{\text{kin},\mathbf{k}} &= - \left\langle \Re \left(\hat{\mathbf{v}}^* \cdot \left[\bar{\bar{P}}_{\mathbf{k}} \cdot (\mathbf{v} \cdot \nabla \mathbf{v}) \right] \right) \right\rangle, \\ \mathcal{T}_{\text{pot},\mathbf{k}} &= - \left\langle \Re \left(\hat{b}^* (\mathbf{v} \cdot \nabla \hat{b}) \right) / N^2 \right\rangle, & \mathcal{B}_{\mathbf{k}} &= - \left\langle \Re \left(\hat{v}_z^* \hat{b} \right) \right\rangle, \\ \varepsilon_{\text{kin},\mathbf{k}} &= (\nu k^2 + \nu_4 k^4) \frac{|\hat{\mathbf{v}}|^2}{2}, & \varepsilon_{\text{pot},\mathbf{k}} &= (\kappa k^2 + \kappa_4 k^4) \frac{|\hat{b}|^2}{2N^2}, \end{aligned} \quad (28)$$

are respectively the kinetic energy injection rate, the kinetic energy transfer, the potential energy transfer, the conversion of kinetic energy to potential energy, the kinetic energy dissipation, and the potential energy dissipation. In the last equations, $(\cdot)^*$ denotes the complex conjugate, $\Re(\cdot)$ the real part, $\langle \cdot \rangle$ stands for the averaging operator, and $\bar{\bar{P}}_{\mathbf{k}} = \mathbb{I} - \mathbf{e}_{\mathbf{k}} \otimes \mathbf{e}_{\mathbf{k}}$ is the projector onto the plane orthogonal to \mathbf{k} . In this section, we study azimuthal average of the energy budget. Namely, we computed quantities like:

$$F(k_h, k_z) = \frac{1}{\Delta k_h \Delta k_z} \sum_{\substack{k_h \leq k'_h < k_h + \Delta k_h \\ k_z \leq |k'_z| < k_z + \Delta k_z}} F_{\mathbf{k}'}, \quad (29)$$

where F can be E_{pot} , E_{polo} , E_{toro} , $E_{\text{kin}} = E_{\text{polo}} + E_{\text{toro}}$, $E = E_{\text{kin}} + E_{\text{pot}}$, \mathcal{T}_{pot} , \mathcal{T}_{kin} , \mathcal{B} , \mathcal{I} , ε_K , or ε_P . Following [20], we use the energy ratios like

$$\frac{E_{\text{toro}}(k_h, k_z)}{E(k_h, k_z)} \quad \text{and} \quad \tilde{\mathcal{D}}(k_h, k_z) = \frac{E_{\text{polo}}(k_h, k_z) - E_{\text{pot}}(k_h, k_z)}{E_{\text{polo}}(k_h, k_z) + E_{\text{pot}}(k_h, k_z)}, \quad (30)$$

in order to quantify the energy content scale by scale. In the same spirit, we also introduce

$$\tilde{\mathcal{T}}_{\text{kin}}(k_h, k_z) = \frac{\mathcal{T}_{\text{kin}}(k_h, k_z)}{\mathcal{T}_{\text{tot}}(k_h, k_z)}, \quad \tilde{\mathcal{T}}_{\text{pot}}(k_h, k_z) = \frac{\mathcal{T}_{\text{pot}}(k_h, k_z)}{\mathcal{T}_{\text{tot}}(k_h, k_z)} \quad \text{and} \quad \tilde{\mathcal{B}}(k_h, k_z) = \frac{\mathcal{B}(k_h, k_z)}{\mathcal{T}_{\text{tot}}(k_h, k_z)}, \quad (31)$$

where

$$\mathcal{T}_{\text{tot}}(k_h, k_z) \equiv |\mathcal{T}_{\text{kin}}(k_h, k_z)| + |\mathcal{T}_{\text{pot}}(k_h, k_z)| + |\mathcal{B}(k_h, k_z)| + \varepsilon_K(k_h, k_z) + \varepsilon_P(k_h, k_z). \quad (32)$$

These quantities are useful for tracking the energy pathways scale by scale. By construction, $\tilde{\mathcal{T}}_{\text{pot}}$, $\tilde{\mathcal{T}}_{\text{kin}}$, and $\tilde{\mathcal{B}}$ vary between -1 and 1 depending on the amplitude and direction of the energy transfer or conversion ($\tilde{\mathcal{B}} > 0$ corresponds to conversion of kinetic energy to potential energy). In a statistically stationary state ($\langle \cdot \rangle = 0$) and in the inertial range ($\mathcal{I}(k_h, k_z) = 0$, $\varepsilon_K(k_h, k_z) \simeq 0$, and $\varepsilon_P(k_h, k_z) \simeq 0$), we should have $\mathcal{T}_{\text{kin}}(k_h, k_z) \simeq -\mathcal{T}_{\text{pot}}(k_h, k_z) \simeq \mathcal{B}(k_h, k_z)$. For this reason, we will present only $\tilde{\mathcal{B}}(k_h, k_z)$.

1. Energy spectra

Figure 5 displays the temporal energy spectra for simulations with $(N, \mathcal{R}_i) = (40, 20)$. In the case where vortical modes are present (Figure 5(a)), we observe that potential and poloidal energies dominate over toroidal energy for frequencies smaller than the Brunt-Väisälä frequency, i.e. $\omega/N < 1$. For $\omega/N \geq 1$, the three components of the energy have very similar spectra. When vortical modes are removed (Figure 5(b)), potential energy is almost in perfect equipartition with poloidal energy at a given frequency. The potential and poloidal energy spectra behave very similarly whether vortical modes are present or not. This might be explained by the fact that vortical modes energy is smaller than potential and poloidal energy at large temporal scales $\omega \leq N$. Interestingly, in Figure 5(b)

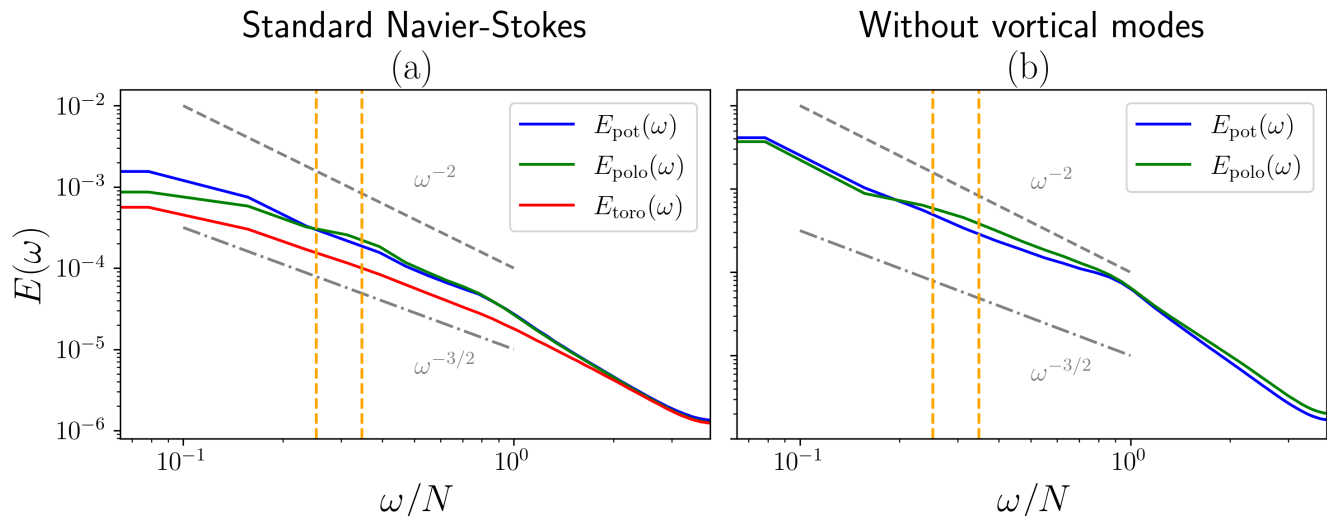


FIG. 5. Temporal energy spectra for simulations $(N, \mathcal{R}_i) = (40, 20)$ with (a) and without (b) vortical modes. The orange dotted lines correspond to the minimal and maximal frequencies of the linear internal gravity waves in the forcing region.

temporal spectra get closer to the Kolmogorov-Zakharov spectra $E(\omega) \sim \omega^{-3/2}$ [5, 37] than the the high frequency limit of the Garrett-Munk spectra $E(\omega) \sim \omega^{-2}$ [72]. The inertial range is larger when vortical modes are removed. Figure 6 shows the 1D integrated spatial spectra, and the normalized (i.e. divided by the total energy dissipation $\varepsilon \equiv \varepsilon_K + \varepsilon_P$) energy fluxes along k_h for the same simulations. We first observe that removing vortical modes does not change the behavior of the poloidal an potential energy spectra (Figure 6(a)-(b)). Up to the the buoyancy wave-vector, the poloidal and potential energies dominate with spectra that are slightly steeper than $k_h^{-5/3}$. After the buoyancy scale (i.e. $k = k_b$), the toroidal energy spectrum starts to be of the same order than the poloidal energy spectrum, which are shallower than $k_h^{-5/3}$. Such changes in the spectral slope around the buoyancy scale were reported in earlier studies [32, 33, 35]. They could be due to shear instabilities occurring at those scales, leading to non-local energy transfers toward small scales [22, 31, 35]. The vertical spectra has a spectral slope between -3 and -2 , which is similar to earlier simulations [36]. Therefore, these 1D spectra do not show strongly stratified turbulence scaling $k_h^{-5/3}$ and k_z^{-3} for $k_b \leq k_h, k_z \leq k_O$ [27, 30]. This might be due to the fact that these simulations do not have a sufficient scale separation between k_b and k_O , which can be attained only at very small F_h [30, 33], or when considering only the largest horizontal scales [36]. Indeed, we observe that vertical spectra tends to be steeper as F_h is decreased, and are steeper than the scaling k_z^{-2} observed in 2D numerical simulations at comparable F_h [70]. The kinetic energy flux $\Pi_{\text{kin}}(k_h)$ and the potential energy flux $\Pi_{\text{pot}}(k_h)$ start to show a plateau over almost a decade in these simulations (Figure 6(c)-(d)). We observe that the dissipation starts to be important at the Ozmidov scale, meaning that these simulations lie between the LAST regime and the viscosity affected regime [31]. This explains why we do not observe an isotropic turbulence range (with energy spectra $\sim k^{-5/3}$) in these simulations. The main effect of removing vortical modes is to make $\Pi_{\text{pot}}(k_h)$ larger than $\Pi_{\text{kin}}(k_h)$. Also, the kinetic energy dissipation $\varepsilon_K(k_h)$ is almost equal to the potential energy dissipation $\varepsilon_P(k_h)$ when vortical modes are removed, as we expect for a system of internal gravity waves with unit Schmidt number [46].

Figure 7 shows slices of the (k_h, k_z) kinetic energy spectrum. The potential and kinetic energy spectra have the same trends with respect to k_h and k_z , so the potential energy spectrum is not presented. As in [20], we observe different scaling laws depending on the region in the (k_h, k_z) plane. Namely, important differences between small k_z and large k_z for a given k_h (Figure 7(a)-(b)):

- For $k_h \ll k_b$, energy is accumulated at the lowest available k_h and small k_z , as usual in stratified turbulence [65, 66, 73]. At $k_z \ll k_b$ the spectra are close to a k_h^{-2} dependency, which is consistent with integrated energy spectra reported in earlier studies [22, 32], but not with the WWT predictions (4). For a fixed $k_z \gg k_b$, we rather observe $E_{\text{kin}} \sim k_h^1$ which would correspond to an equipartition of energy in horizontal scales.
- For $k_h \gg k_b$, the spectrum starts to depend less and less on k_z , and the $E_{\text{kin}}(k_h, k_z)$ slices eventually merge around $k_h \sim k_O$, when the eddy turnover time becomes less than the period of any linear waves, i.e. $\chi_{\mathbf{k}} > 1$.

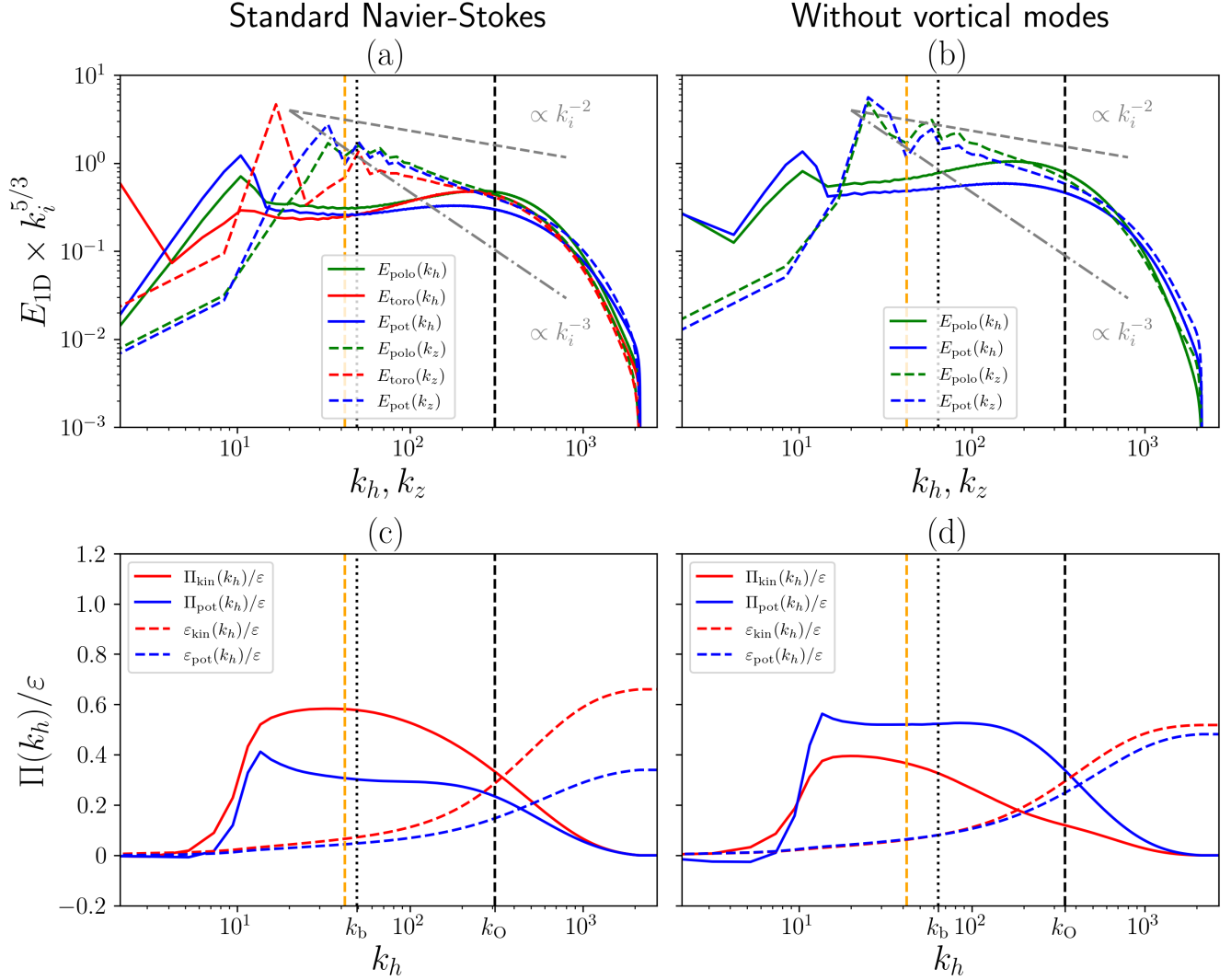


FIG. 6. Compensated 1D spatial energy spectra for simulations $(N, \mathcal{R}_i) = (40, 20)$ with (a) and without (b) vortical modes. Normalized k_h energy fluxes for the same simulations with (c) and without (d) vortical modes. The orange dotted line corresponds to the maximal wave-vector modulus of the forcing region, the black dotted line to k_b , the black dashed line to k_O .

Important differences can also be noted when looking at k_z slices (Figure 7(c)-(d)):

- For $k_z \ll k_b$, the spectrum is close to $\sim k_z^0$, indicating that horizontal layers of height larger than the buoyancy scale are in equipartition of energy in these strongly stratified simulations.
- For $k_b \ll k_z \ll k_O$, the spectrum is very steep at small horizontal wave-vectors, while it remains flat at large horizontal wave-vectors.
- For $k_z \gg k_O$, the spectral slope starts to depend less and less on k_h . Yet, the $E_{\text{kin}}(k_h, k_z)$ does not merge around $k_h \sim k_O$ since small horizontal scales are more energetic compared to the large horizontal scales.

Due to the reduced aspect ratio of our simulations, we do not observe a net separation between the forcing and the buoyancy scales. Still, the kinetic energy spectrum remains very similar to the one presented in [20]. Interestingly, the trends of the kinetic energy spectra appear to be very similar, regardless of whether vortical modes are present or not. This is a first indication that the presence of vortical modes is not the only obstacle to observing internal gravity wave turbulence in realistic flows.

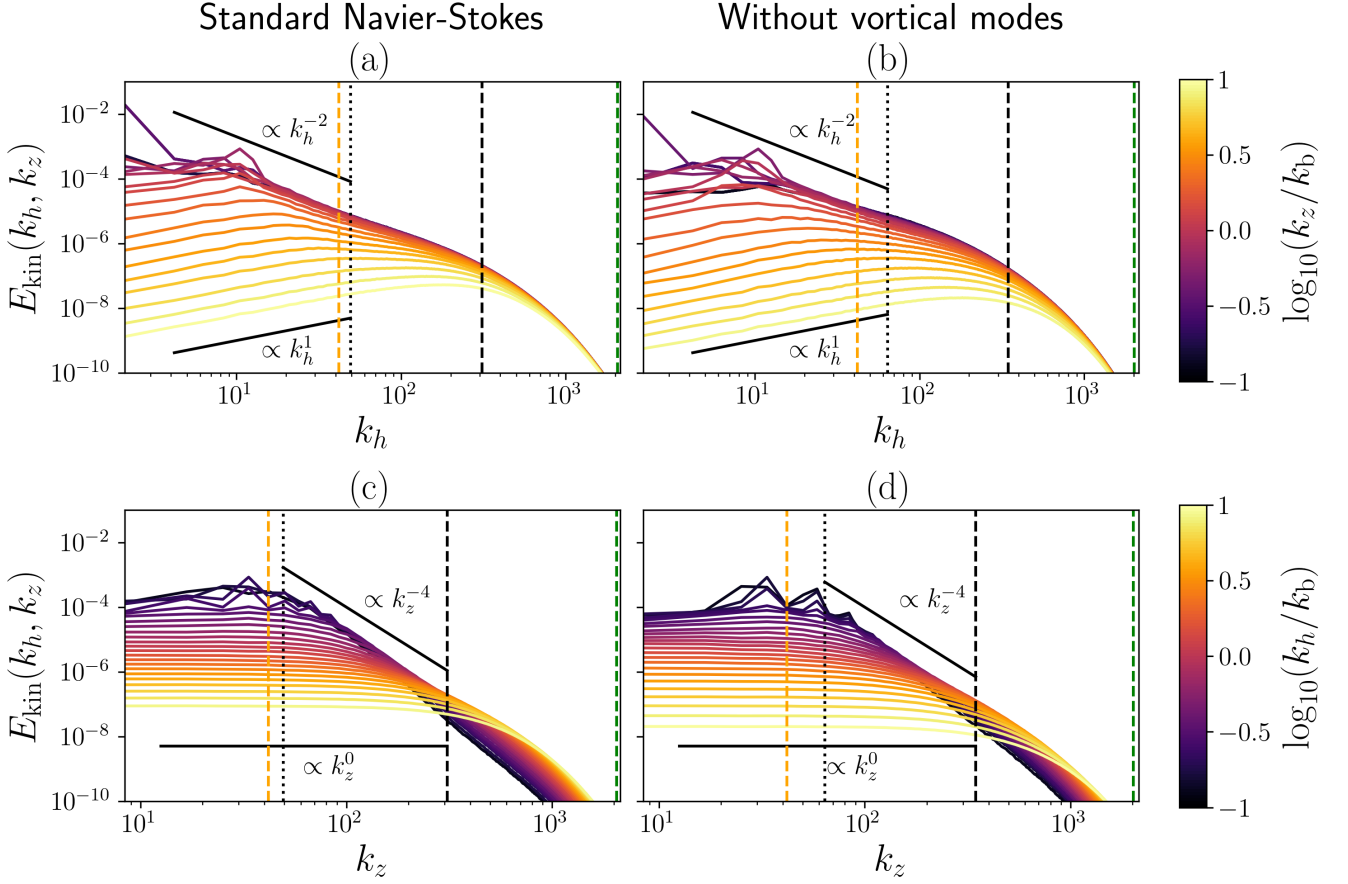


FIG. 7. Slices of the kinetic energy spectrum $E_{\text{kin}}(k_h, k_z)$ for simulations $(N, \mathcal{R}_i) = (40, 20)$ with and without vortical modes. The orange dotted line corresponds to the maximal wave-vector modulus of the forcing region, the black dotted line to k_b , the black dashed line to k_O , and the green dashed line to the dissipative wave-vector. (a) E_{kin} vs k_h with vortical modes. (b) E_{kin} vs k_h without vortical modes. (c) E_{kin} vs k_z with vortical modes. (d) E_{kin} vs k_z without vortical modes.

Figure 8 shows the (k_h, k_z) spectra. Obviously, the simulation without vortical modes has no energy in the toroidal velocity. When vortical modes are present, an important part of the energy is contained in one vortical mode with $(k_h, k_z) = (\Delta k_h, 2\Delta k_z)$, corresponding to large, nearly vertically stacked shear layers (Figure 8(a)). Energy then tends to be accumulated at the smallest horizontal wave vectors, close to shear modes. When vortical modes are removed, energy is still concentrated in the same wave-vectors, but in the form of poloidal and potential energy (Figure 8(d)-(f)). Except for this qualitative difference, the toroidal, poloidal, and potential energy spectra show the same trends.

In order to have a finer analysis of the distribution of energy in the (k_h, k_z) plane, it is useful to look at energy ratios E_{toro}/E and $\tilde{\mathcal{D}}$ (24) shown on Figure 9. One clearly observes that E_{toro} is never negligible away from the forcing region, and it is very important for small wave-vectors when the vortical modes are not removed (Figure 9(a)-(b)). Apart from this important difference, the spectral energy budgets of the two simulations appear to share striking similarities. Outside the forcing region, the poloidal energy is dominant ($\tilde{\mathcal{D}} > 0$) between the cyan dotted lines $\chi_{\mathbf{k}} = 1/3$ and $\chi_{\mathbf{k}} = 3$ (25), corresponding to a region where the critical balance condition $\chi_{\mathbf{k}} \sim 1$ is fulfilled (Figure 9(c)-(d)). The potential energy is dominant ($\tilde{\mathcal{D}} < 0$) when $\chi_{\mathbf{k}} > 3$, i.e. in a region where eddies are faster than waves. We observe a good equipartition between potential and poloidal energy ($\tilde{\mathcal{D}} \simeq 0$) when $\chi_{\mathbf{k}} < 1/3$, i.e. in the region where waves are faster than eddies. This indicates that the ratio of temporal scales $\chi_{\mathbf{k}}$ is important when identifying ranges in anisotropic turbulence, as already explained in [20]. In particular, it shows that a wave dominated range cannot lie above $\chi_{\mathbf{k}} > 1/3$.

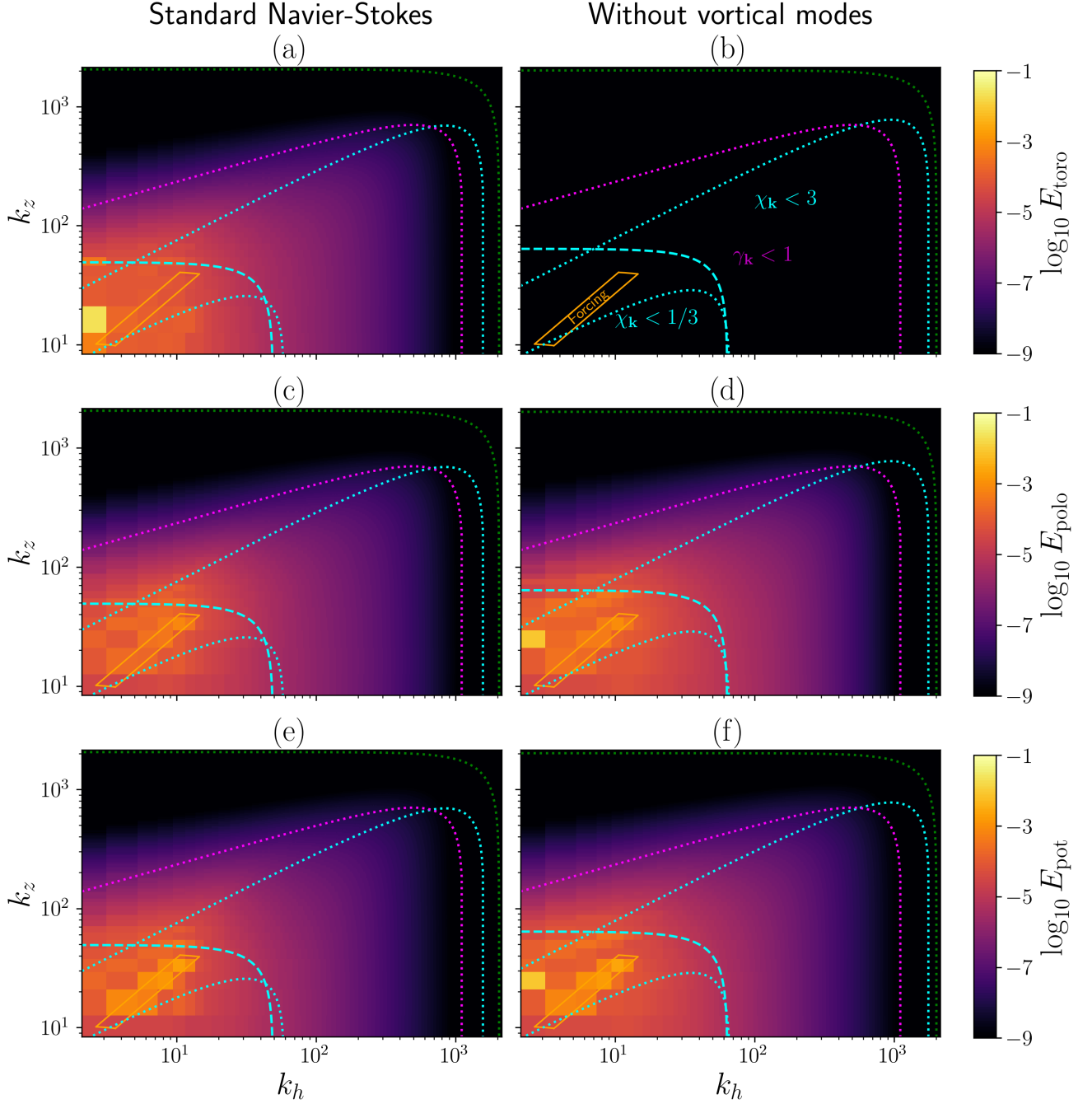


FIG. 8. (k_h, k_z) spectra for the simulations at $(N, \mathcal{R}_i) = (40, 20)$, with and without vortical modes. The cyan dotted lines correspond to $\chi_k = 1/3$ and $\chi_k = 3$, the cyan dashed line to $k = k_b$, the magenta dotted line to $\gamma_k = 1$, and the green dotted line to the dissipative scale. The orange box corresponds to the forcing region. (a) E_{toro} with vortical modes. (b) E_{toro} without vortical modes. (c) E_{polo} with vortical modes. (d) E_{polo} without vortical modes. (e) E_{pot} with vortical modes. (f) E_{pot} without vortical modes.

2. Conversion of kinetic to potential energy

We can observe, in Figure 10, that the conversion between potential energy and kinetic energy $\tilde{\mathcal{B}}$ is very similar with or without vortical modes. This is not surprising since the vertical velocity is fully contained in waves modes, and not in vortical modes. Naturally, the amplitude of $\tilde{\mathcal{B}}$ is important only when $\gamma_k < 1$, meaning that waves need to not be

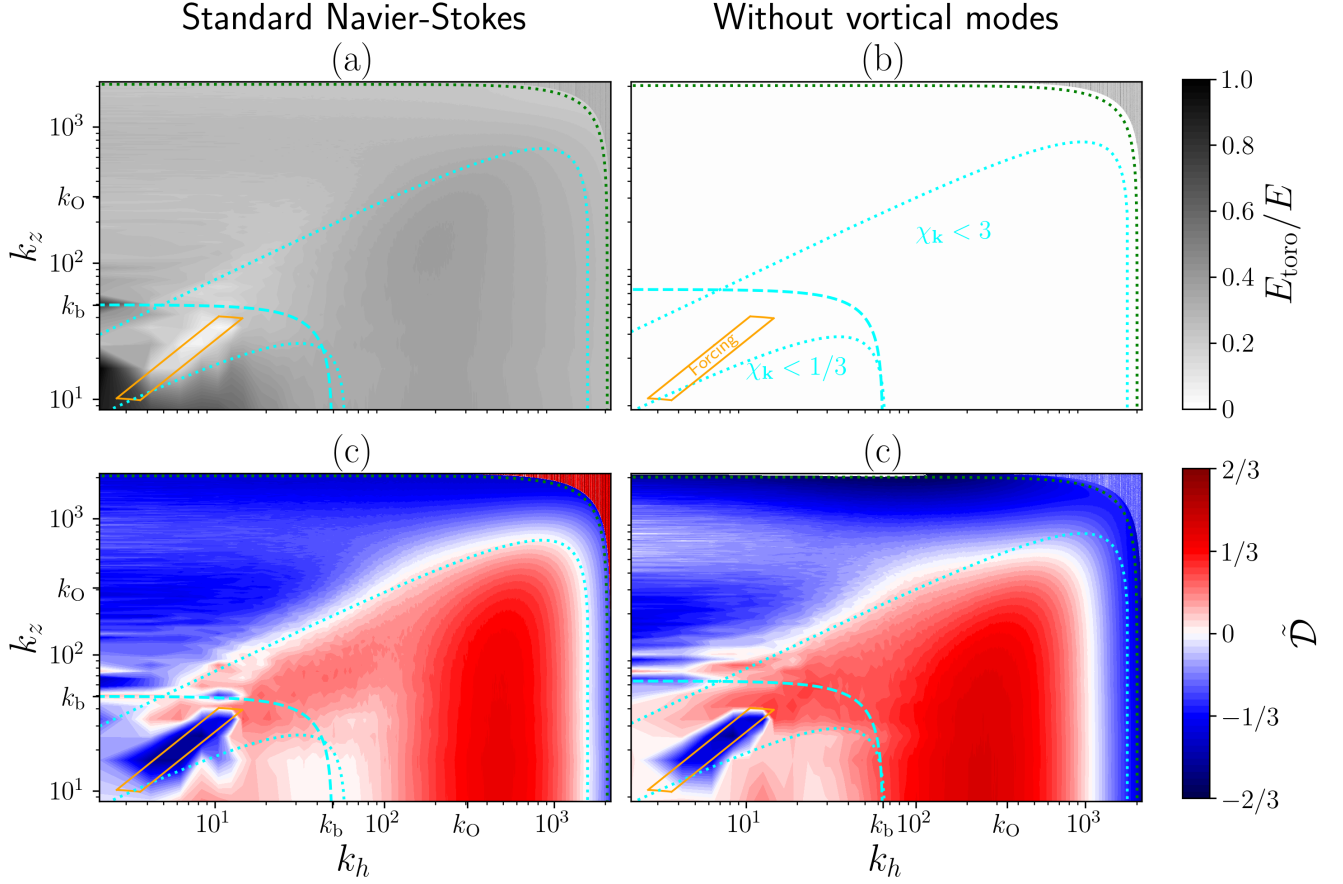


FIG. 9. Ratios of energy for the simulations at $(N, \mathcal{R}_i) = (40, 20)$, with and without vortical modes. The cyan dotted lines correspond to $\chi_k = 1/3$ and $\chi_k = 3$, the cyan dashed line to $k = k_b$, and the green dotted line to the dissipative scale. The orange box corresponds to the forcing region. (a) E_{toro}/E with vortical modes. (b) E_{toro}/E without vortical modes. (c) $\tilde{D} = (E_{\text{polo}} - E_{\text{pot}})/(E_{\text{polo}} + E_{\text{pot}})$ with vortical modes. (d) \tilde{D} without vortical modes. A wave dominated region is expected for the simulation without vortical where $\chi_k < 1/3$, for which $E_{\text{toro}} = 0$ and $\tilde{D} \ll 1$.

damped too strongly by viscosity or diffusivity in order to convert potential energy to kinetic energy (or conversely). Yet, we observe that \tilde{B} is non-zero and has a definite sign when $\gamma_k > 1$. Consequently, if waves certainly exist in this range, they cannot persist because their kinetic energy is converted into potential energy or vice-versa. Therefore, these simulations are unlikely to correspond to a WWT regime, even in the buoyancy range and without vortical modes. Nevertheless, we observe that \tilde{B} fluctuates in time in the buoyancy range ($k \leq k_b$).

C. Spatiotemporal analysis in the buoyancy range

From the previous subsection, it is expected that waves can dominate (but cannot necessarily sustain) not too far from the buoyancy range ($k \leq k_b$). To further assess the presence and degree of nonlinearity of waves, we performed a spatiotemporal analysis for small k . As explained in the previous subsection, waves are marked by an equipartition between poloidal kinetic energy and potential energy. This motivates us to introduce the equipartition energy as

$$E_{\text{equi}}(k_h, k_z) = 2 \min \{E_{\text{polo}}(k_h, k_z), E_{\text{pot}}(k_h, k_z)\}, \quad (33)$$

in order to track the presence of waves in the (k_h, k_z) plane. Indeed, E_{equi} corresponds to the energy contained in E_{pot} and E_{polo} that is in potential-kinetic equipartition. Consequently, E_{equi} encompass the energy of the waves. However, it is important to note that E_{equi} can also contain the energy of structures that are not linear waves. A more careful separation between waves and non-wave structures requires a 4D spatiotemporal filtering [41, 42], which

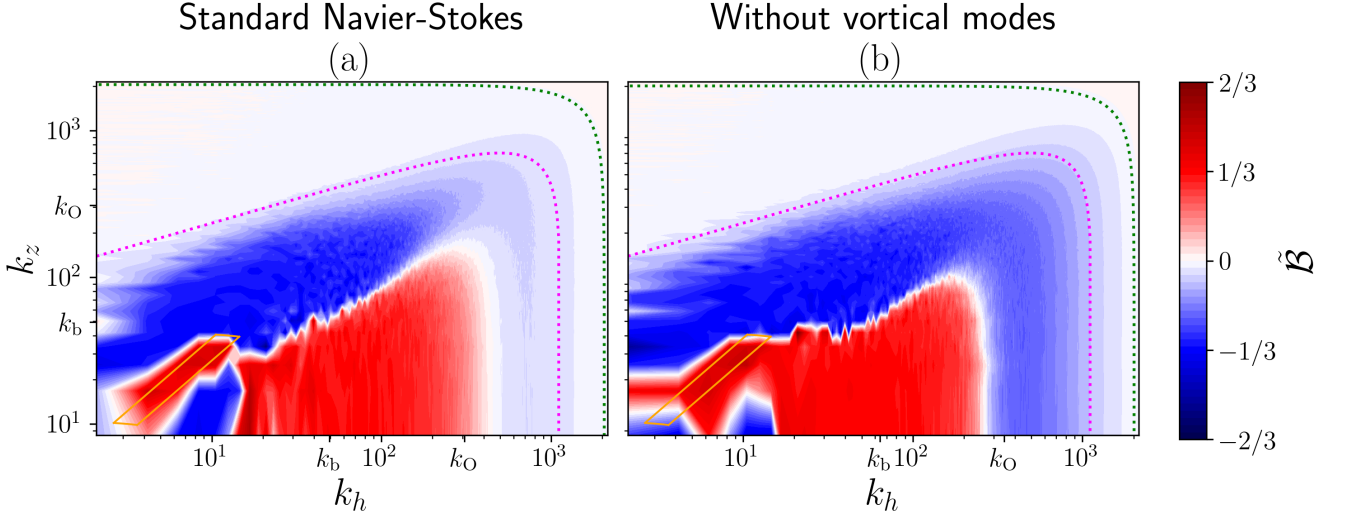


FIG. 10. Normalized conversion to potential energy \tilde{B} (31) for the simulations at $(N, \mathcal{R}_i) = (40, 20)$, with (a) and without (b) vortical modes. The magenta dotted line corresponds to $\gamma_{\mathbf{k}} = 1$, and the green dotted line to the dissipative scale. The orange box corresponds to the forcing region.

is expensive in term of computational time and data storage. Yet, the ratio $E_{\text{equi}}(k_h, k_z)/E(k_h, k_z)$ can be used to track waves in the spectral space at a lower cost.

Figure 11 shows slices of the temporal spectrum of the equipartition energy $E_{\text{equi}}(k_h, k_z, \omega)$ at large spatial scales, namely $k_h = 25.1$ and $k_z = 25.1$. We observe that the energy tends to be concentrated around the linear wave frequency only at large spatial scales, but is dispersed at smaller scales even in the simulations without vortical modes. It has been shown that this dispersion could be quantified by considering a Doppler effect due to the advection of internal waves by shear modes [40]. Despite the fact that shear modes are removed in our simulations, we can try to test this prediction by considering that a Doppler shift is due to a horizontal mean flow \mathbf{U} of amplitude U_h

$$\delta\omega_{\text{doppler}} = \max_{\varphi_{\mathbf{k}}} \mathbf{U} \cdot \mathbf{k} = kU_h \sin \theta_{\mathbf{k}} = \frac{k}{k_b} \omega_{\mathbf{k}} \quad (34)$$

where $\varphi_{\mathbf{k}}$ is the angle between the horizontal projection of \mathbf{k} and \mathbf{e}_x (Figure 1). This gives a reasonable explanation of the important dispersion of the energy in temporal scale at large horizontal wave-vectors (Figure 11).

To observe more precisely the dispersion in temporal scales, we represent the ratio $E_{\text{equi}}(k_h, k_z, \omega)/\max_{\omega} E(k_h, k_z, \omega)$ for some (k_h, k_z) on Figure 12, which indicates how the energy is distributed among temporal scales for a given spatial scale. For a system of weakly nonlinear internal gravity waves, we should observe a peak of $E_{\text{equi}}/\max_{\omega} E$ around $\omega = \omega_{\mathbf{k}}$ (for the energy to be concentrated around the linear frequency), whose maxima should be close to unity (for the energy to be concentrated in waves modes). We observe that the concentration of energy around the linear frequency mostly depends on the ratio k/k_b . As expected, the pics of energy around $\omega = \omega_{\mathbf{k}}$ is more pronounced when $k \ll k_b$. This is an indication that linear waves are important if $k \ll k_b$, with or without vortical modes. When $k \simeq k_b$, the energy spreads over a broader range of temporal scales. We note that removing vortical modes from the dynamics helps to concentrate E_{equi} in temporal scales since temporal spectra tend to be more sharp. Simulations without vortical modes naturally have bigger $E_{\text{equi}}/\max_{\omega} E$ (Figure 12(b)) when compared to simulations with vortical modes (Figure 12(a)).

A way to measure the dispersion of energy in temporal scales is to compute the deviation from linear waves frequency $\delta\omega$. We estimate it using the equipartition energy spectrum and defining the following measure,

$$\delta\omega(k_h, k_z) = \sqrt{\frac{\sum_{\omega} (\omega - \omega_{\mathbf{k}})^2 E_{\text{equi}}(k_h, k_z, \omega)}{\sum_{\omega} E_{\text{equi}}(k_h, k_z, \omega)}}. \quad (35)$$

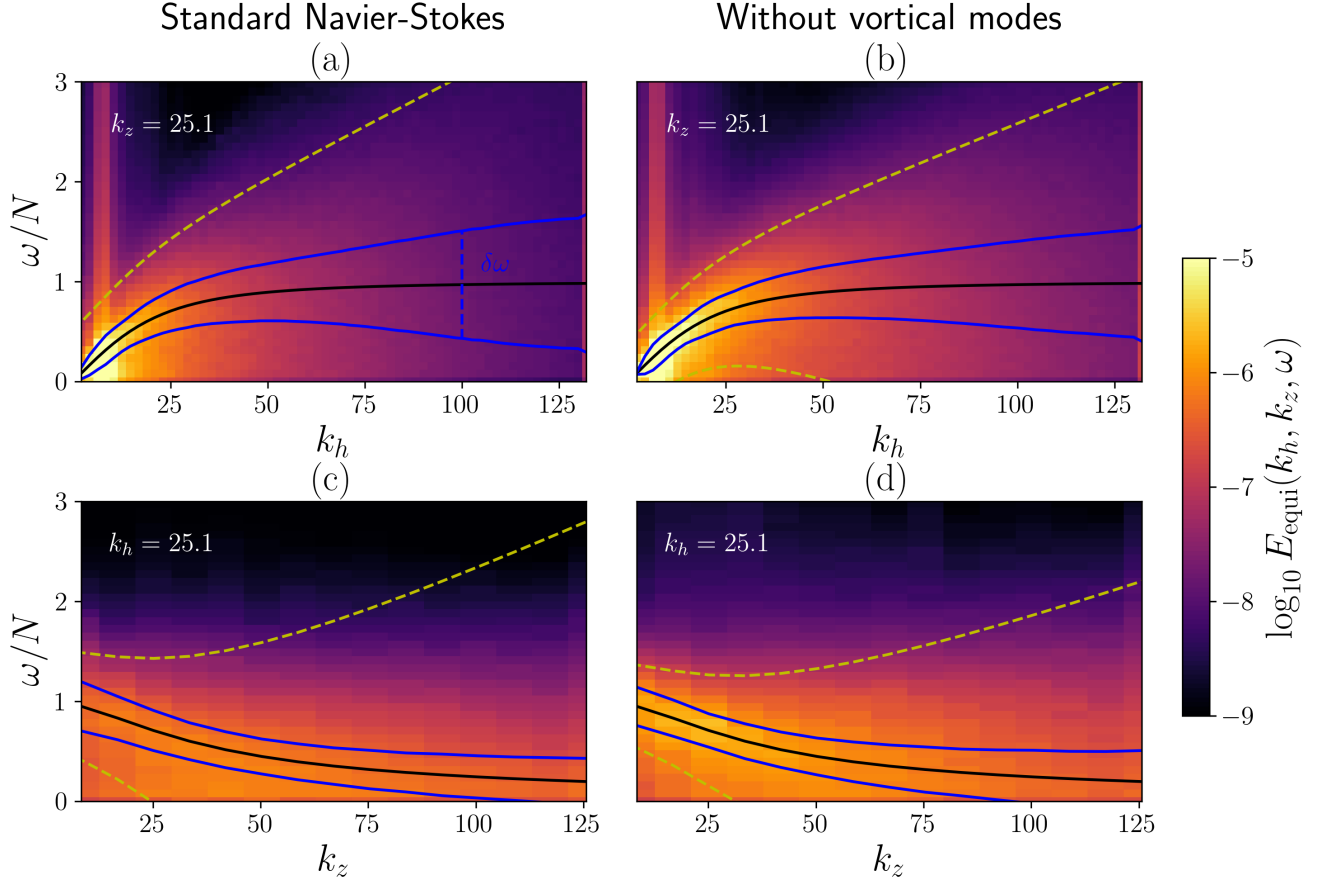


FIG. 11. Slices of $E_{\text{equi}}(k_h, k_z, \omega)$ for the simulations at $(N, \mathcal{R}_i) = (40, 20)$, with and without vortical modes. (a) $k_z = 25.1$ with vortical modes. (b) $k_z = 25.1$ without vortical modes. (c) $k_h = 25.1$ with vortical modes. (d) $k_h = 25.1$ without vortical modes. The linear dispersion relation $\omega_{\mathbf{k}} = Nk_h/k$ is plotted in black, the lines $\omega_{\mathbf{k}} \pm \delta\omega/2$ (35) in blue, and the yellow dashed lines correspond to the lines $\omega_{\mathbf{k}} \pm \delta\omega_{\text{doppler}}$ (34).

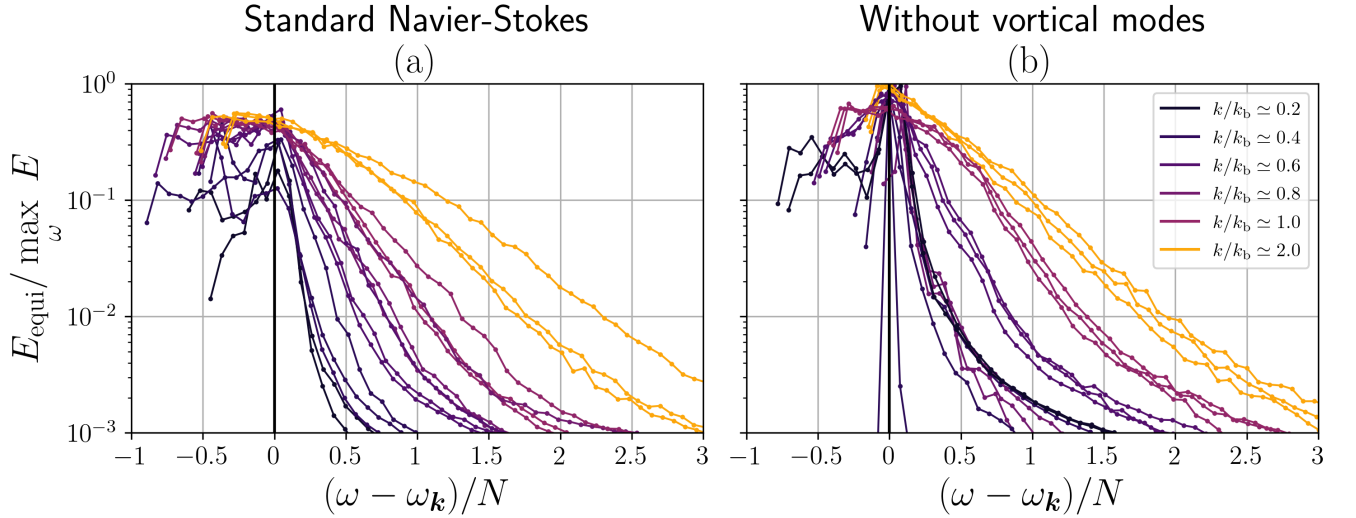


FIG. 12. Spatiotemporal analysis of the simulations with $(N, \mathcal{R}_i) = (40, 20)$. $E_{\text{equi}}(k_h, k_z, \omega) / \max_{\omega} E(k_h, k_z, \omega)$ for the simulation with vortical modes (a) and for the simulation without vortical modes (b). Only some couples (k_h, k_z) are shown. Line colors corresponds to different values of k/k_b . The vertical black lines corresponds to $\omega = \omega_{\mathbf{k}}$.

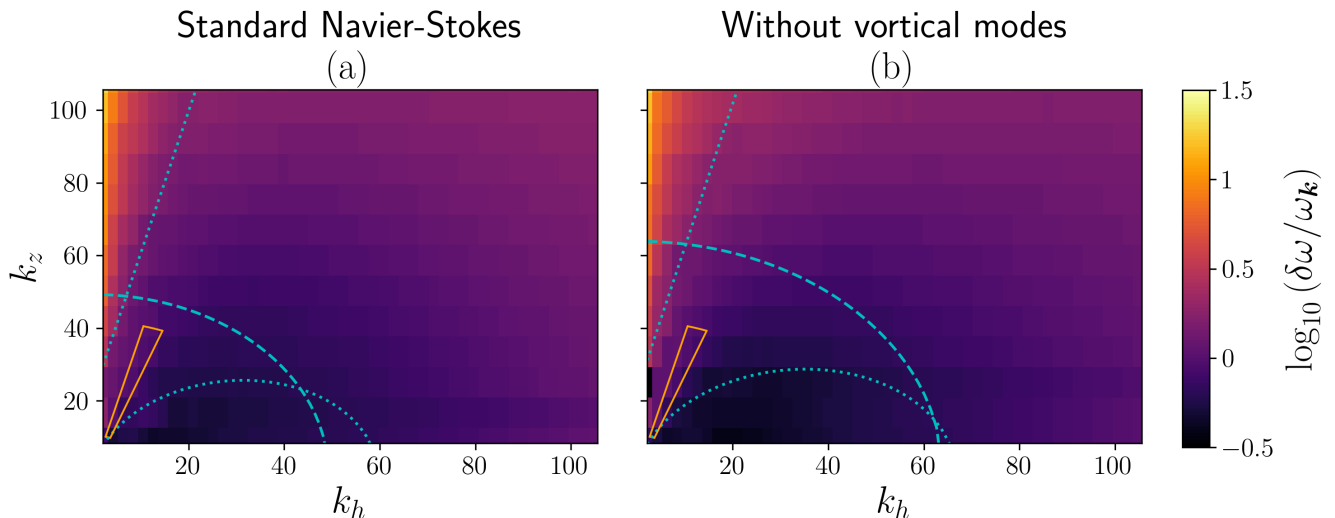


FIG. 13. $\delta\omega/\omega_{\mathbf{k}}$ for simulations with $(N, \mathcal{R}_i) = (40, 20)$ with vortical modes (a) and without vortical modes (b). Dotted lines correspond to $\chi_{\mathbf{k}} = 1/3$ and $\chi_{\mathbf{k}} = 3$, the dashed line to $k = k_b$, and the orange box to the forcing region.

The quantity $\delta\omega/\omega_{\mathbf{k}}$ is another way to estimate the strength of nonlinear interactions. Unlike the nonlinearity parameter $\chi_{\mathbf{k}}$, which is defined by dimensional analysis, $\delta\omega/\omega_{\mathbf{k}}$ requires knowledge of the spatio-temporal spectra. $\delta\omega/\omega_{\mathbf{k}}$ is called nonlinear broadening, and is particularly important in the context of WWT: for $\delta\omega/\omega_{\mathbf{k}} \gg 1$, waves' dynamics is strongly affected by nonlinear interactions, while when $\delta\omega/\omega_{\mathbf{k}} \ll 1$, waves can propagate with only weak nonlinear perturbations and the theory can hold [2]. For a system of non-interacting linear waves, $\delta\omega/\omega_{\mathbf{k}}$ should be zero. Figure 13 shows this quantity in the (k_h, k_z) plane. It shows that the nonlinear broadening is small if $k \ll k_b$ and $\chi_{\mathbf{k}} \leq 1/3$, which is consistent with previous results [20]. Conversely, $\delta\omega/\omega_{\mathbf{k}}$ is large when $k \gg k_b$ or $\chi_{\mathbf{k}} > 3$. We observed that removing vortical tends to decrease slightly $\delta\omega/\omega_{\mathbf{k}}$ at small k and large $\theta_{\mathbf{k}}$. This might be explained by the fact that the simulations without vortical modes tend to have a larger buoyancy range when compared to the simulations with vortical modes.

In order to allow a continuum of interaction between waves, it is also important that the nonlinear broadening remains much larger than the frequency gap between discrete modes in the Fourier space [14]. This leads to the condition $\Delta\omega \equiv \nabla_{\mathbf{k}}\omega_{\mathbf{k}} \cdot \Delta\mathbf{k} \ll \delta\omega$ where $\Delta\mathbf{k} = (\Delta k_x, \Delta k_y, \Delta k_z)$. Taking $\Delta k_x = \Delta k_y = \Delta k_z = \Delta k$ leads to $|\cos\theta_{\mathbf{k}}|\Delta k/k \ll \delta\omega/N$, which is satisfied in most of our simulations for sufficiently large k .

D. Wave energy in the parameters space

The previous subsections presented the dispersion in temporal scales for two simulations, but we did not quantify the amount of waves in the (k_h, k_z) plane, nor in the (F_h, \mathcal{R}) plane so far. This is the goal of this subsection.

To discuss the effect of stratification, we show the integrated spatiotemporal total energy spectra as a function of $\theta_{\mathbf{k}}/N = \sin\theta_{\mathbf{k}}$ and ω for different simulations in Figure 14. At low N , we observe no big difference in $E(\omega_{\mathbf{k}}, \omega)$ between simulations with and without vortical modes (Figure 14(a)-(b)). We observe that, for these weakly stratified flows, the energy is mostly contained in small frequency modes, but present over a large range of temporal scales for a given angle of the wave-vector $\theta_{\mathbf{k}}$. At larger N , energy concentrate around the linear dispersion relation $\omega = \omega_{\mathbf{k}}$ and in slow modes $\omega = 0$ for simulation with vortical modes (Figure 14(c)). When vortical modes are absent, energy tends to accumulate around $\omega = \omega_{\mathbf{k}}$ only (Figure 14(d)). At the highest N , the two branches $\omega = \omega_{\mathbf{k}}$ and $\omega = 0$ are visible for the simulation with vortical modes (Figure 14(e)) while only the branches $\omega = \omega_{\mathbf{k}}$ is clearly observed in the simulation without vortical modes (Figure 14(f)).

In order to quantify wave energy in a flow, we propose to simply filter the spatiotemporal spectra E_{equi} by a Gaussian weight with mean $\omega_{\mathbf{k}}$ and root-mean-square $\epsilon\omega_{\mathbf{k}}$, where ϵ is an arbitrary but small parameter, such that the wave

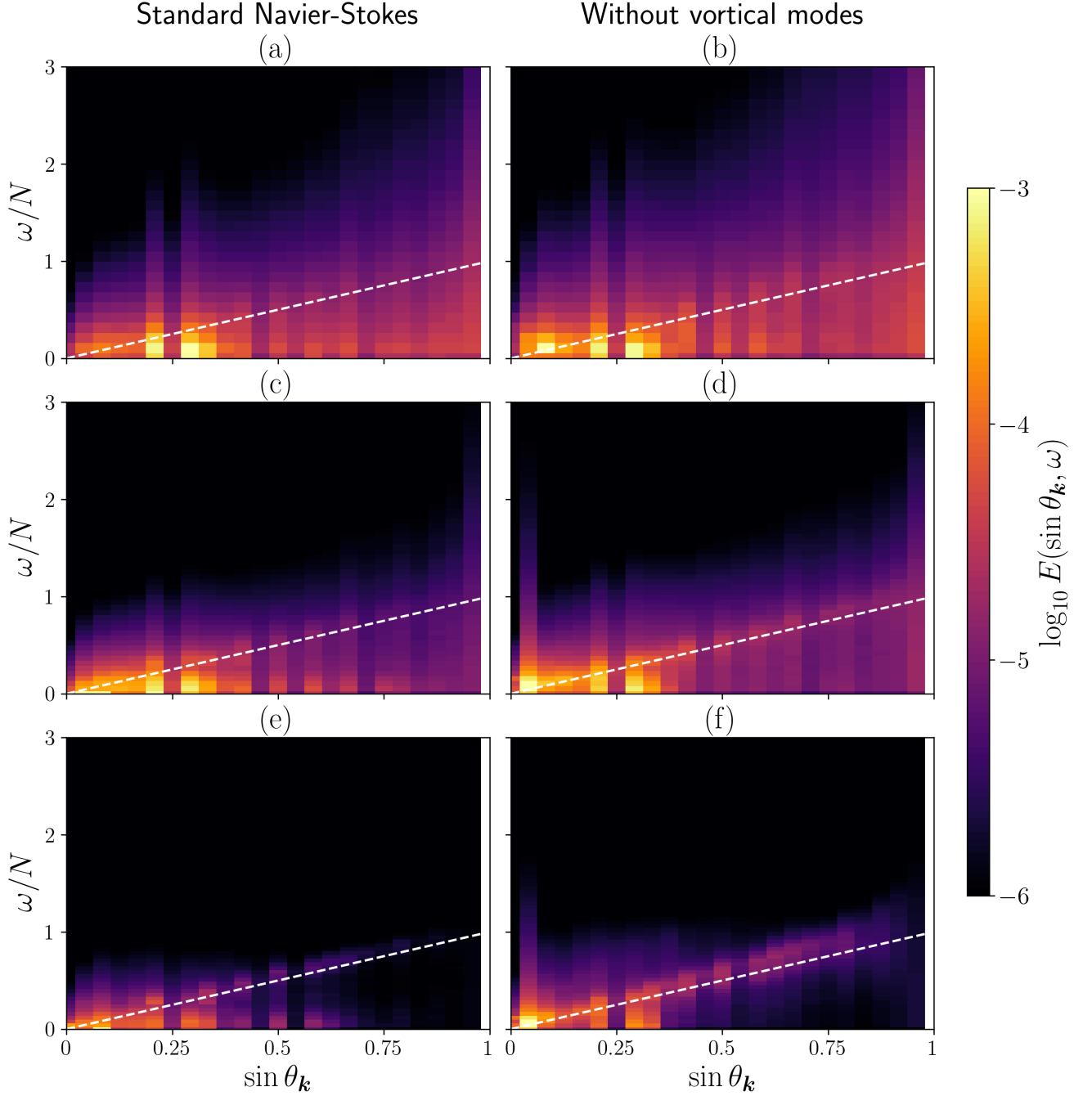


FIG. 14. Integrated spatiotemporal spectra of the total energy as a function of $\omega_{\mathbf{k}}/N = \sin \theta_{\mathbf{k}}$ and ω for different simulations at the same viscosity $\nu = 1/(N^2 \mathcal{R}_i)$. (a) $(N, \mathcal{R}_i) = (20, 160)$ with vortical modes, (b) $(N, \mathcal{R}_i) = (20, 160)$ without vortical modes, (c) $(N, \mathcal{R}_i) = (40, 40)$ with vortical modes, (d) $(N, \mathcal{R}_i) = (40, 40)$ without vortical modes, (e) $(N, \mathcal{R}_i) = (80, 10)$ with vortical modes, and (f) $(N, \mathcal{R}_i) = (80, 10)$ without vortical modes. The white dotted line represents $\omega = \omega_{\mathbf{k}}$, i.e. the linear dispersion relation.

energy at a given (k_h, k_z, ω) is

$$E_{\text{wave}}(k_h, k_z, \omega) = E_{\text{equi}}(k_h, k_z, \omega) \exp \left[-\frac{1}{2} \left(\frac{\omega - \omega_{\mathbf{k}}(k_h, k_z)}{\epsilon \omega_{\mathbf{k}}(k_h, k_z)} \right)^2 \right]. \quad (36)$$

We observed that choosing $\epsilon = 0.1$ gives a sufficiently narrow window to keep only the spatiotemporal region corre-

sponding to internal gravity waves, while keeping the window sufficiently wide to avoid binning effects. Therefore, we kept this value for the analysis. This window with variable width allows us to get rid of the energy of non-wave structures at low frequency. We first look at the distribution of the wave energy in the (k_h, k_z) plane. In order to allow a fair comparison between simulations with and without vortical modes, it is necessary to introduce the wave energy ratio

$$\tilde{E}_{\text{wave}}(k_h, k_z) = \frac{E_{\text{wave}}(k_h, k_z)}{E_{\text{polo}}(k_h, k_z) + E_{\text{pot}}(k_h, k_z)} \quad \text{where} \quad E_{\text{wave}}(k_h, k_z) = \sum_{\omega} E_{\text{wave}}(k_h, k_z, \omega). \quad (37)$$

Normalizing the wave energy by the total energy (i.e. including vortical modes energy) would have mask the presence of waves in the simulation with vortical modes, since they represent an important part of the energy (Figure 9(a)). The wave energy ratio $\tilde{E}_{\text{wave}}(k_h, k_z)$ is depicted on Figure 15(a)-(b). We observe that \tilde{E}_{wave} tends to be higher for simulations without vortical modes, but removing vortical modes does not change the variations of \tilde{E}_{wave} in the (k_h, k_z) plane for these simulations. As we could have expected from previous works [20] and the previous subsections, \tilde{E}_{wave} is higher in the buoyancy range, in particular where $\chi_{\mathbf{k}} \leq 1/3$. Yet, \tilde{E}_{wave} tends to be bigger at very specific angles, smaller than the forcing angle θ_f . This accumulation of internal gravity wave energy at specific propagation angles has been reported in earlier studies (see e.g. [40]). In the present simulations, we can explain this by invoking Triadic Resonance Instabilities (TRI) between internal gravity waves [43], in particular the PSI [53, 56]. Considering that a primary wave of frequency $\omega_f = \omega_0^* = N \sin \theta_f$ is excited by the forcing, and then decays into two daughter waves of the same frequency ω_1^* according to the PSI mechanism, we can deduce ω_1^* and the associated propagation angle θ_1^* :

$$\omega_1^* = \frac{\omega_0^*}{2} = 0.15 N \quad \Rightarrow \quad \theta_1^* = \arcsin\left(\frac{\omega_1^*}{N}\right) \simeq 0.15. \quad (38)$$

Invoking, for a second time, the PSI mechanism for a wave of frequency ω_1^* , we can deduce a second harmonic

$$\omega_2^* = \frac{\omega_1^*}{2} = 0.075 N \quad \Rightarrow \quad \theta_2^* = \arcsin\left(\frac{\omega_2^*}{N}\right) \simeq 0.075. \quad (39)$$

A third harmonic is obtained by considering that two waves of frequencies ω_1^* and ω_2^* interact to give a third wave with frequency

$$\omega_3^* = \omega_1^* + \omega_2^* = 0.225 N \quad \Rightarrow \quad \theta_3^* = \arcsin\left(\frac{\omega_3^*}{N}\right) \simeq 0.225. \quad (40)$$

θ_f , θ_1^* , θ_2^* , and θ_3^* are reported on Figure 15(a)-(b). We see that they reproduce well with the higher values of \tilde{E}_{wave} observed at small angles. This agreement suggests that waves at small frequencies are excited by TRI in our strongly stratified simulations.

The spatiotemporal analysis performed in this subsection allows to give a more precise measure of the dominance of waves in the spectral space at a given (F_h, \mathcal{R}) . The total wave energy ratio is defined as

$$\tilde{E}_{\text{wave}} = \frac{\sum_{k_h, k_z, \omega} E_{\text{wave}}(k_h, k_z, \omega)}{\sum_{k_h, k_z} E_{\text{polo}}(k_h, k_z) + E_{\text{pot}}(k_h, k_z)}. \quad (41)$$

Figure 16 shows \tilde{E}_{wave} in the plane (F_h, \mathcal{R}) . Consistently with the previous subsections, we observe that removing the vortical modes helps to get higher values of \tilde{E}_{wave} , and thus, in principle, to get closer to a WWT regime. Yet, unstratified flows ($F_h \geq 1$) have almost no energy in waves modes (i.e. $E_{\text{wave}} \ll 1$), and increasing the stratification (decreasing F_h) is required to increase the wave energy ratio (Figures 16(a) and 14), but it also tends to increase the vortical mode energy (Figure 3(a)) when they are not artificially removed from the dynamics. Figure 16(b) shows that \tilde{E}_{wave} tends to decrease with \mathcal{R} for sufficiently low F_h . This is consistent with the numerical simulations of stratified flows forced by tides [46], which show convincing signatures of a WWT regime at relatively small \mathcal{R} when compared to more usual strongly stratified simulations. Some of our simulations at low F_h and high \mathcal{R} remain affected by hyperviscosity, so \mathcal{R} may not accurately quantify the effect of dissipation in this case. However, discarding these simulations from the analysis still leads to the same conclusions.

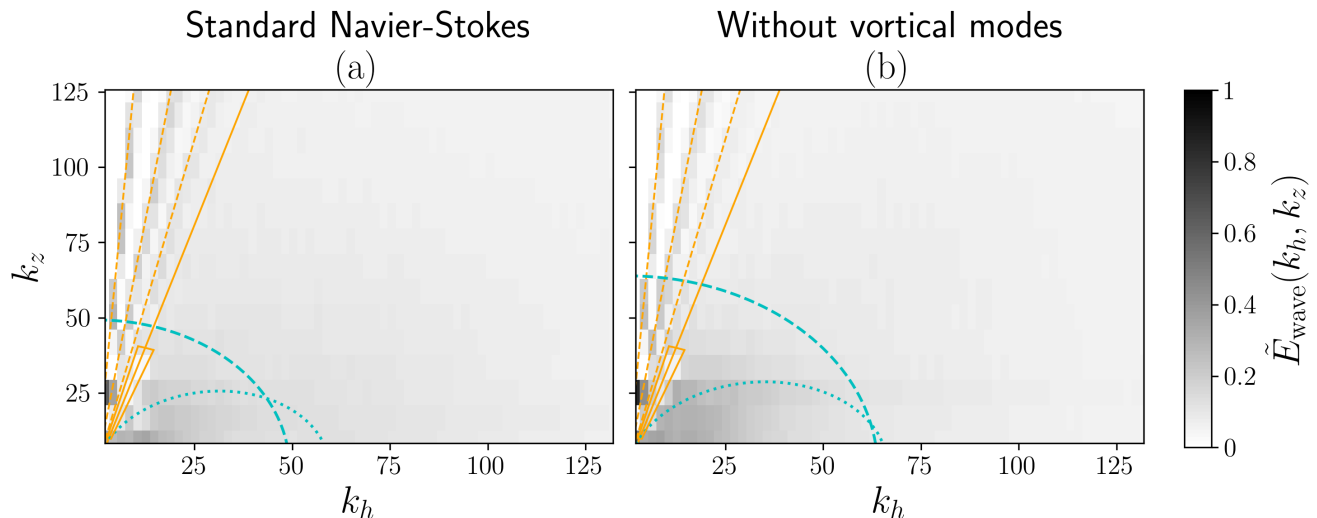


FIG. 15. Wave energy ratio $\tilde{E}_{\text{wave}}(k_h, k_z)$ (37) for simulations with $(N, \mathcal{R}_i) = (40, 20)$ with vortical modes (a), and without vortical modes (b). The cyan dotted lines correspond to $\chi_{\mathbf{k}} = 1/3$, and the cyan dashed line to $k = k_b$. The orange box corresponds to the forcing region. The forcing angle θ_f is represented by a full orange line, while first harmonics (38-40) excited by the TRI are indicated by dashed orange lines.

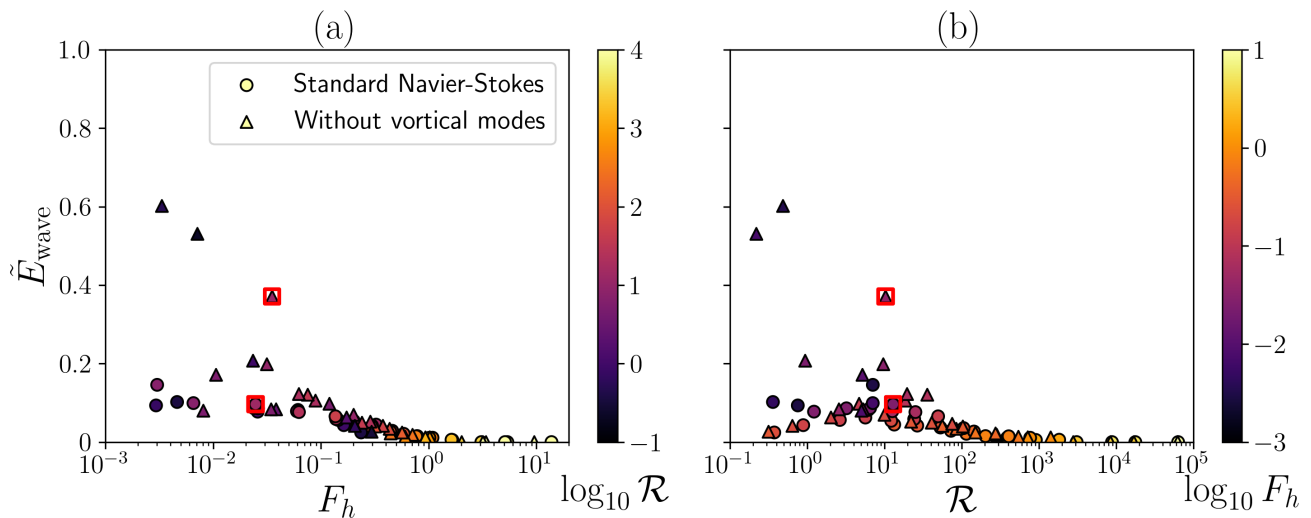


FIG. 16. \tilde{E}_{wave} as a function of F_h (a) and \mathcal{R} (b) for all our simulations with or without vortical modes. The red boxes indicate the simulations with $(N, \mathcal{R}_i) = (40, 20)$ investigated in the previous subsections.

IV. DISCUSSIONS AND CONCLUSIONS

In order to investigate the conditions under which a weak internal gravity wave turbulence regime could occur, we performed direct numerical simulations of stratified turbulence without shear modes, and with or without vortical modes, at various Froude and buoyancy Reynolds numbers.

We observed that removing vortical modes helps to have a better overall balance between poloidal kinetic energy and potential energy. However, the spatial spectra appear to behave very similarly with or without vortical modes in our simulations. The spectral energy budget reveals that there is no range in (k_h, k_z) for which the conversion between kinetic energy and potential energy fluctuates around zero, as we would expect for a system of statistically stationary waves. Additionally, the conversion between potential energy and kinetic energy becomes small where the

wave dissipation parameter $\gamma_{\mathbf{k}}$ (26) is larger than unity. Due to the anisotropy of stratified flows, this means that it exists a range of scales where waves are efficiently dissipated by viscosity, but not necessarily the vortices.

A spatiotemporal analysis in the buoyancy range showed that increasing stratification is necessary to decrease the nonlinear broadening to the level required for a weak wave turbulence regime. As in [20], we observed that waves are present in a region delimited by the nonlinearity parameter $\chi_{\mathbf{k}}$ (25). More precisely, waves are more likely to dominate where $\chi_{\mathbf{k}} < 1/3$, if the vortical modes are removed. We also observed evidences of the presence of slow waves ($k_z \gg k_h$) subject to TRI where $\chi_{\mathbf{k}} \geq 1/3$ in simulations with or without vortical modes. However, the nonlinear broadening is shown to be large for $k_z \gg k_h$, so slow waves are less susceptible to be described by the WWT theory. Although removing vortical modes is not enough to observe a weak wave turbulence regime, simulations without vortical modes produce $E(\omega_{\mathbf{k}}, \omega)$ plots (Figure 14) characterized by a better concentration of energy in wave modes. Additionally, temporal spectra of strongly stratified simulations without vortical modes exhibit a larger inertial range in temporal scales (Figure 5). The spectra are also compatible with the Kolmogorov-Zakharov spectrum offered by WWT. However, this spectrum is known to be mathematically unrealizable, so the agreement between this prediction and our simulations remains to be explained.

Using a simple diagnostic to quantify wave energy contained in a stratified flow, we showed that that the buoyancy Reynolds number should not be too large in order to observe a WWT regime. To understand this, we propose the following conditions in order to limit the generation of non wave structures and to ensure the weak nonlinearity for the evolution of all energetic modes:

- The waves and eddies should be dissipated in the buoyancy range which leads to the conditions

$$k_d \leq k_b \quad \Rightarrow \quad \mathcal{R} \leq F_h \quad \text{and} \quad k_\eta \leq k_b \quad \Rightarrow \quad \mathcal{R} \leq F_h^{2/3}. \quad (42)$$

if we assume that dissipation of eddies occurs at the Kolmogorov wave-vector $k_\eta = (\varepsilon_\kappa/\nu^3)^{1/4}$. These conditions are necessary to avoid wave breaking and the development of 3D small-scale eddies.

- The nonlinearity parameter $\chi_{\mathbf{k}}$ should remain small for all energetic modes. If we assume that dissipation occurs at $k \lesssim k_\eta$, this leads to the condition

$$\chi_{\max} \equiv \max_{\mathbf{k}} \chi_{\mathbf{k}} \leq 1 \quad \Rightarrow \quad \max_{\mathbf{k}} \frac{1}{\sin \theta_{\mathbf{k}}} \left(\frac{k}{k_O} \right)^{2/3} = \frac{k_\eta}{k_{h,\min}} \left(\frac{k_\eta}{k_O} \right)^{2/3} \leq 1 \quad (43)$$

where $k_{h,\min}$ represents the minimal horizontal wave-vector. If we consider a flow of finite size with no shear modes, $k_{h,\min} = 2\pi/L_h$ such that

$$\chi_{\max} = \frac{k_\eta L_h}{2\pi} \left(\frac{k_\eta}{k_O} \right)^{2/3} \leq 1 \quad \Rightarrow \quad \left(\frac{\varepsilon_\kappa L_h^4}{\nu^3} \right)^{1/4} \mathcal{R}^{1/2} \lesssim 1. \quad (44)$$

Finally, we require the flow to be in a fully turbulent regime such that

$$Re = \mathcal{R} F_h^{-2} \gg 1 \quad \text{and} \quad \varepsilon_\kappa \sim U_h^3/L_h. \quad (45)$$

Then, substituting the definition of Re from equation (10) and condition (45) into equation (44) yields

$$\mathcal{R} \lesssim F_h^{6/5}. \quad (46)$$

To summarize, we propose that a weak internal gravity waves turbulence regime could occur only if F_h and \mathcal{R} are such that conditions (42), (45), and (46) are fulfilled. Note that the last thresholds are obtained by dimensional analysis, so they are defined up to dimensionless factors, which are set to one for simplicity. On Figure 17, we plot our simulations in the (F_h, \mathcal{R}) plane, as well as the simulations of [31, 42, 46, 74] and some recent experiments [45]. For the simulations of [46], the Froude number is computed using our definition (10), and the buoyancy Reynolds number as $\mathcal{R} = Re F_h^2$ in order to compare to our work. Namely, we have used Table 1 in [46] with $U_h = u_{\text{rms}}$, $\varepsilon_\kappa = \varepsilon_k$, and $Re = Re_0$. This leads to different values of F_h and \mathcal{R} than the ones presented by the authors. We observe that our simulations do not lie in the region corresponding to (42), (45), and (46). On the contrary, [46] attained such a region in their simulations, which provides a tangible explanation for why they obtained better signatures of WWT. It is worth mentioning that [46] did not have to remove shear nor vortical modes in their simulations to observe signatures of internal wave turbulence. It indicates that there must be some threshold below which both shear and vortical

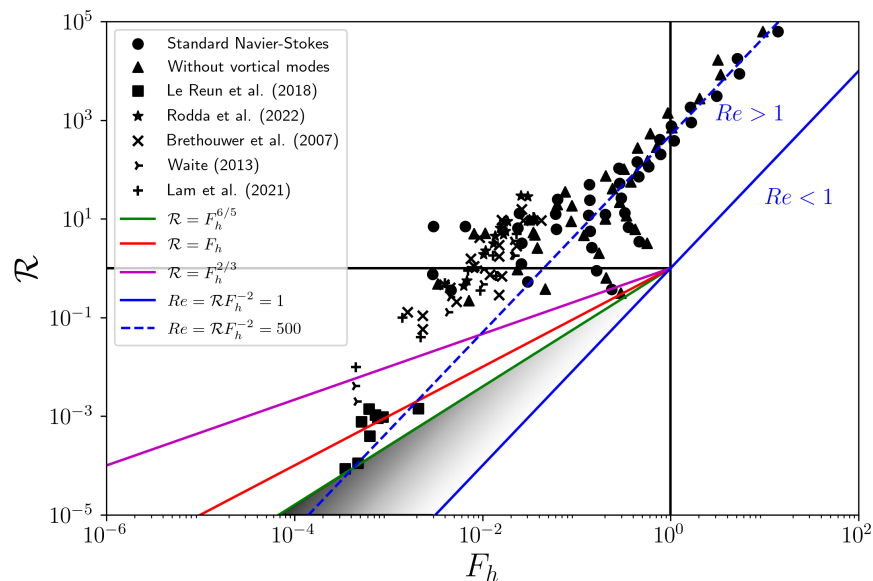


FIG. 17. Simulations of the present study and [31, 42, 46, 74], and the experiments [45] in the (F_h, \mathcal{R}) parameters space. The colored full lines corresponding to conditions (42), (45), and (46) (see legend). The blue dashed line corresponds to $Re = 500$. The colored region is where a weak wave turbulence regime is expected.

modes do not grow if not directly forced. Such a situation would be analogous to rotating flows where there is a threshold below which geostrophic modes do not grow [49]. We observe that [74] also attained very small \mathcal{R} . In this study, the authors forced vortical modes so their simulations are not well suited for WWT. Yet, they showed that potential enstrophy tends to be quadratic (i.e. $V \simeq V_2$) for $F_h, \mathcal{R} \ll 1$ and that $V_2 \propto \int \Omega_z^2 dx dy dz$ increases with \mathcal{R} in their simulations. It suggests that vortical modes energy increases with \mathcal{R} when $\mathcal{R} \lesssim 1$, as explained by [42]. Yet, the study of the wave energy ratio is not done while keeping F_h or \mathcal{R} constant in [42]. To our knowledge, additional studies are needed to confirm if the wave energy ratio is for $\mathcal{R} \ll 1$ and $F_h \ll 1$ a decreasing function of \mathcal{R} , and if a threshold below which both shear and vortical modes are stable exists.

If the latter claims are true, they constitute very prohibitive conditions for observing WWT in numerical simulations and experiments. To illustrate this point, let us consider a turbulent flow at $Re = 10^3$ that typically requires a $\sim 1024^3$ resolution. Then (46) stipulates that the flow need to attain $F_h \leq Re^{-5/4} = 1.78 \times 10^{-4}$ for the nonlinearity parameter to be small for all energetic modes. Yet, the kinetic time for a system of internal gravity waves is expected to grow as F_h^{-2} , meaning that very long simulations are required to attain the steady state, even for relatively small domains.

ACKNOWLEDGMENTS

We thank two anonymous reviewers for their constructive feedback. This project was supported by the Simons Foundation through the Simons collaboration on wave turbulence. Part of the computations have been done on the “Mesocentre SIGAMM” machine, hosted by Observatoire de la Côte d’Azur. The authors are grateful to the OPAL infrastructure from Université Côte d’Azur and the Université Côte d’Azur’s Center for High-Performance Computing for providing resources and support. This work was granted access to the HPC/AI resources of IDRIS under the allocation 2022-A0122A13417 made by GENCI.

Appendix A: Forcing scheme

Our forcing is designed to excite waves and computed via generation of pseudo random numbers with uniform distribution and time interpolation. Namely, we use the following algorithm:

$t = 0; t_0 = 0;$
 Generate two complex random fields $\hat{f}_0(\mathbf{k})$ and $\hat{f}_1(\mathbf{k});$
 $\hat{\mathbf{f}} = \hat{f}_0 \mathbf{e}_{p\mathbf{k}};$
 Normalize $\hat{\mathbf{f}}$ to ensure $P_K(t) = \sum_{\mathbf{k}} \Re \left[\hat{\mathbf{f}} \cdot \hat{\mathbf{v}}^* + \frac{\Delta t}{2} |\hat{\mathbf{f}}|^2 \right] = 1;$
while $t \leq T$ **do**
 $t = t + \Delta t;$
 if $t - t_0 \geq T_c$ **then**
 $t_0 = t;$
 $\hat{f}_0 = \hat{f}_1;$
 Generate $\hat{f}_1;$
 end
 $\hat{\mathbf{f}} = \left\{ \hat{f}_0 - \frac{(\hat{f}_1 - \hat{f}_0)}{2} \left[\cos \left(\frac{\pi(t - t_0)}{T_c} \right) + 1 \right] \right\} \mathbf{e}_{p\mathbf{k}};$
 Normalize $\hat{\mathbf{f}};$
end

where Δt is the time increment at each time step and T is the final time of the simulation. The random complex fields are built such that their inverse Fourier transform is real and they are null for unforced wavenumbers.

Appendix B: List of simulations

TABLE I. Overview of the numerical and physical parameters used in the simulations. $\mathcal{R}_i = P_K/\nu N^2$. F_h and \mathcal{R} are the turbulent horizontal Froude number and buoyancy Reynolds number, respectively, defined in (10).

Control parameters			With vortical modes				Without vortical modes			
N	\mathcal{R}_i	L_h/L_z	n_h	$k_{\max}\eta$	F_h	\mathcal{R}	n_h	$k_{\max}\eta$	F_h	\mathcal{R}
0.25	64000	2	640	1.07	1.38e+01	63655	640	1.07	9.55e+00	62857
0.66	9000	2	640	1.09	5.37e+00	8858	640	1.10	3.40e+00	8472
0.66	18000	2	1280	1.29	5.10e+00	17761	1280	1.31	3.19e+00	17019
1.12	3200	2	640	1.07	3.08e+00	3090	640	1.10	2.02e+00	2791
2	1000	2	640	1.09	1.66e+00	915	640	1.16	1.02e+00	719
2	2000	2	1280	1.30	1.63e+00	1834	1280	1.38	9.31e-01	1425
3	450	2	640	1.10	1.08e+00	389	640	1.18	7.07e-01	286
3	900	2	1280	1.30	1.01e+00	772	1280	1.42	6.05e-01	544
4	250	2	640	1.12	7.83e-01	204	640	1.21	5.66e-01	151
4	500	2	1280	1.33	7.64e-01	407	1280	1.47	4.43e-01	275
5.20	150	2	640	1.13	5.86e-01	115	640	1.21	4.34e-01	85.6
6.50	100	2	640	1.11	4.58e-01	72.9	640	1.18	3.76e-01	56.4
6.50	200	2	1280	1.32	4.40e-01	144	1280	1.43	3.18e-01	104
10	5	2	320	2.78	4.64e-01	3.5	320	2.83	5.63e-01	3.2
10	10	2	320	1.66	3.55e-01	6.8	320	1.70	4.20e-01	6.2
10	20	2	640	1.98	3.24e-01	13.4	320	1.03	3.40e-01	11.7
10	40	2	640	1.18	2.98e-01	26.6	640	1.24	2.87e-01	22.2
10	80	2	1280	1.40	2.87e-01	53.2	640	0.75	2.40e-01	41.0
10	160	2	1280	0.84	2.80e-01	106	1280	0.91	2.04e-01	75.5
14.5	20	2	640	1.16	2.01e-01	12.3	640	1.22	2.01e-01	10.0
20	1	4	640	7.66	2.36e-01	0.4	640	8.00	2.95e-01	0.3
20	2	4	640	4.37	1.63e-01	0.9	640	4.73	2.06e-01	0.6
20	5	4	640	2.10	1.45e-01	2.7	640	2.25	1.73e-01	2.0
20	10	4	1280	2.46	1.39e-01	5.7	1280	2.57	1.20e-01	4.7
20	20	4	1280	1.44	1.35e-01	11.9	1280	1.55	8.75e-02	9.0
20	40	4	1280	0.85	1.38e-01	24.3	1280	0.91	8.89e-02	18.7
20	80	4	1920	0.76	1.36e-01	49.6	1280	0.55	7.53e-02	35.9
30	10	4	1280	1.31	6.12e-02	6.2	1280	1.40	3.58e-02	4.7
30	20	4	1920	1.16	5.97e-02	12.7	1280	0.83	3.14e-02	9.7
30	40	4	1280	0.46	6.24e-02	25.2	1280	0.49	6.24e-02	19.7
40	1	4	640	2.48	3.01e-02	0.5	640	2.70	4.64e-02	0.4
40	2	4	640	1.42	2.58e-02	1.2	640	1.52	2.34e-02	0.9
40	5	4	1280	1.42	2.60e-02	3.2	1280	1.50	3.83e-02	2.6
40	10	4	1280	0.84	2.38e-02	6.5	1280	0.88	3.45e-02	5.3
40	20	4	2560	1.00	2.47e-02	13.0	2560	1.06	3.52e-02	10.4
60	10	4	1280	0.45	6.54e-03	7.1	1280	0.48	1.06e-02	5.2
80	0.5	8	640	1.37	4.61e-03	0.4	640	1.55	7.13e-03	0.2
80	1	8	640	0.80	2.94e-03	0.8	640	0.90	3.33e-03	0.5
80	10	8	2560	0.58	3.01e-03	7.1	2560	0.63	8.09e-03	5.0

-
- [1] V. E. Zakharov, V. S. L'vov, and G. Falkovich, *Kolmogorov Spectra of Turbulence I*, Springer Series in Nonlinear Dynamics (Springer, 1992).
- [2] S. Nazarenko, *Wave Turbulence*, Lecture Notes in Physics, Vol. 825 (Springer, 2011).
- [3] S. Nazarenko, *Wave turbulence*, Contemporary Physics **56**, 359 (2015), publisher: Taylor & Francis .eprint: <https://doi.org/10.1080/00107514.2015.1015250>.
- [4] E. Falcon and N. Mordant, Experiments in surface gravity–capillary wave turbulence, Annual Review of Fluid Mechanics **54**, 1 (2022), .eprint: <https://doi.org/10.1146/annurev-fluid-021021-102043>.
- [5] P. Caillol and V. Zeitlin, Kinetic equations and stationary energy spectra of weakly nonlinear internal gravity waves, Dynamics of Atmospheres and Oceans **32**, 81 (2000).
- [6] S. Galtier, Weak inertial-wave turbulence theory, Physical Review E **68**, 015301 (2003), publisher: American Physical Society.

- [7] S. B. Medvedev and V. Zeitlin, Turbulence of near-inertial waves in the continuously stratified fluid, *Physics Letters A* **371**, 221 (2007).
- [8] A. Griffin, G. Krstulovic, V. S. L'vov, and S. Nazarenko, Energy spectrum of two-dimensional acoustic turbulence, *Physical Review Letters* **128**, 224501 (2022), publisher: American Physical Society.
- [9] G. Düring, C. Josserand, and S. Rica, Weak turbulence for a vibrating plate: Can one hear a kolmogorov spectrum?, *Physical Review Letters* **97**, 025503 (2006), publisher: American Physical Society.
- [10] S. Galtier, S. V. Nazarenko, A. C. Newell, and A. Pouquet, A weak turbulence theory for incompressible magnetohydrodynamics, *Journal of Plasma Physics* **63**, 447 (2000), publisher: Cambridge University Press.
- [11] V. S. L'vov and S. Nazarenko, Weak turbulence of kelvin waves in superfluid he, *Low Temperature Physics* **36**, 785 (2010), publisher: American Institute of Physics.
- [12] S. Dyachenko, A. C. Newell, A. Pushkarev, and V. E. Zakharov, Optical turbulence: weak turbulence, condensates and collapsing filaments in the nonlinear schrödinger equation, *Physica D: Nonlinear Phenomena* **57**, 96 (1992).
- [13] S. Galtier and S. V. Nazarenko, Turbulence of weak gravitational waves in the early universe, *Physical Review Letters* **119**, 221101 (2017), publisher: American Physical Society.
- [14] V. S. L'vov and S. Nazarenko, Discrete and mesoscopic regimes of finite-size wave turbulence, *Phys. Rev. E* **82**, 056322 (2010).
- [15] L. Biven, S. V. Nazarenko, and A. C. Newell, Breakdown of wave turbulence and the onset of intermittency, *Physics Letters A* **280**, 28 (2001).
- [16] B. Miquel and N. Mordant, Nonstationary wave turbulence in an elastic plate, *Physical Review Letters* **107**, 034501 (2011), publisher: American Physical Society.
- [17] N. Yokoyama and M. Takaoka, Identification of a separation wave number between weak and strong turbulence spectra for a vibrating plate, *Physical Review E* **89**, 012909 (2014), publisher: American Physical Society.
- [18] Y. Pan and D. K. Yue, Direct numerical investigation of turbulence of capillary waves, *Physical Review Letters* **113**, 094501 (2014), publisher: American Physical Society.
- [19] Y. Zhu, B. Semisalov, G. Krstulovic, and S. Nazarenko, Testing wave turbulence theory for the gross-pitaevskii system, *Physical Review E* **106**, 014205 (2022), publisher: American Physical Society.
- [20] N. Yokoyama and M. Takaoka, Energy-based analysis and anisotropic spectral distribution of internal gravity waves in strongly stratified turbulence, *Physical Review Fluids* **4**, 104602 (2019), publisher: American Physical Society.
- [21] N. Yokoyama and M. Takaoka, Energy-flux vector in anisotropic turbulence: application to rotating turbulence, *Journal of Fluid Mechanics* **908**, A17 (2021), publisher: Cambridge University Press.
- [22] M. L. Waite, Stratified turbulence at the buoyancy scale, *Physics of Fluids* **23**, 066602 (2011), publisher: American Institute of Physics.
- [23] C. Staquet and J. Sommeria, INTERNAL GRAVITY WAVES: From instabilities to turbulence, *Annual Review of Fluid Mechanics* **34**, 559 (2002), eprint: <https://doi.org/10.1146/annurev.fluid.34.090601.130953>.
- [24] G. K. Vallis, *Atmospheric and Oceanic Fluid Dynamics: Fundamentals and Large-Scale Circulation*, 2nd ed. (Cambridge University Press, 2017).
- [25] J. A. MacKinnon, Z. Zhao, C. B. Whalen, A. F. Waterhouse, D. S. Trossman, O. M. Sun, L. C. S. Laurent, H. L. Simmons, K. Polzin, R. Pinkel, A. Pickering, N. J. Norton, J. D. Nash, R. Musgrave, L. M. Merchant, A. V. Melet, B. Mater, S. Legg, W. G. Large, E. Kunze, J. M. Klymak, M. Jochum, S. R. Jayne, R. W. Hallberg, S. M. Griffies, S. Diggs, G. Danabasoglu, E. P. Chassignet, M. C. Buijsman, F. O. Bryan, B. P. Briegleb, A. Barna, B. K. Arbic, J. K. Ansong, and M. H. Alford, Climate process team on internal wave-driven ocean mixing, *Bulletin of the American Meteorological Society* **98**, 2429 (2017), publisher: American Meteorological Society Section: Bulletin of the American Meteorological Society.
- [26] M. Gregg, E. D'Asaro, J. Riley, and E. Kunze, Mixing efficiency in the ocean, *Annual Review of Marine Science* **10**, 443 (2018), eprint: <https://doi.org/10.1146/annurev-marine-121916-063643>.
- [27] P. Billant and J.-M. Chomaz, Self-similarity of strongly stratified inviscid flows, *Physics of Fluids* **13**, 1645 (2001), publisher: American Institute of Physics.
- [28] M. L. Waite and P. Bartello, Stratified turbulence dominated by vortical motion, *Journal of Fluid Mechanics* **517**, 281 (2004), publisher: Cambridge University Press.
- [29] M. L. Waite and P. Bartello, Stratified turbulence generated by internal gravity waves, *Journal of Fluid Mechanics* **546**, 313 (2006), publisher: Cambridge University Press.
- [30] E. Lindborg, The energy cascade in a strongly stratified fluid, *Journal of Fluid Mechanics* **550**, 207 (2006), publisher: Cambridge University Press.
- [31] G. Brethouwer, P. Billant, E. Lindborg, and J.-M. Chomaz, Scaling analysis and simulation of strongly stratified turbulent flows, *Journal of Fluid Mechanics* **585**, 343 (2007), publisher: Cambridge University Press.
- [32] Y. Kimura and J. R. Herring, Energy spectra of stably stratified turbulence, *Journal of Fluid Mechanics* **698**, 19 (2012), publisher: Cambridge University Press.
- [33] P. Bartello and S. M. Tobias, Sensitivity of stratified turbulence to the buoyancy reynolds number, *Journal of Fluid Mechanics* **725**, 1 (2013), publisher: Cambridge University Press.
- [34] A.-M. E. G. Brunner-Suzuki, M. A. Sundermeyer, and M.-P. Lelong, Upscale energy transfer by the vortical mode and internal waves, *Journal of Physical Oceanography* **44**, 2446 (2014), publisher: American Meteorological Society Section: Journal of Physical Oceanography.

- [35] P. Augier, P. Billant, and J.-M. Chomaz, Stratified turbulence forced with columnar dipoles: numerical study, *Journal of Fluid Mechanics* **769**, 403 (2015), publisher: Cambridge University Press.
- [36] A. Maffioli, Vertical spectra of stratified turbulence at large horizontal scales, *Physical Review Fluids* **2**, 104802 (2017), publisher: American Physical Society.
- [37] Y. V. Lvov and E. G. Tabak, Hamiltonian formalism and the garrett-munk spectrum of internal waves in the ocean, *Physical Review Letters* **87**, 168501 (2001), publisher: American Physical Society.
- [38] G. Dematteis and Y. V. Lvov, Downscale energy fluxes in scale-invariant oceanic internal wave turbulence, *Journal of Fluid Mechanics* **915**, A129 (2021), publisher: Cambridge University Press.
- [39] G. Dematteis, K. Polzin, and Y. V. Lvov, On the origins of the oceanic ultraviolet catastrophe, *Journal of Physical Oceanography* **52**, 597 (2022), publisher: American Meteorological Society Section: Journal of Physical Oceanography.
- [40] A. Maffioli, A. Delache, and F. S. Godeferd, Signature and energetics of internal gravity waves in stratified turbulence, *Physical Review Fluids* **5**, 114802 (2020), publisher: American Physical Society.
- [41] H. Lam, A. Delache, and F. S. Godeferd, Partitioning waves and eddies in stably stratified turbulence, *Atmosphere* **11**, 420 (2020), number: 4 Publisher: Multidisciplinary Digital Publishing Institute.
- [42] H. Lam, A. Delache, and F. S. Godeferd, Energy balance and mixing between waves and eddies in stably stratified turbulence, *Journal of Fluid Mechanics* **923**, A31 (2021), publisher: Cambridge University Press.
- [43] C. Brouzet, Internal wave attractors : from geometrical focusing to non-linear energy cascade and mixing (2016).
- [44] G. Davis, T. Jamin, J. Deleuze, S. Joubaud, and T. Dauxois, Succession of resonances to achieve internal wave turbulence, *Physical Review Letters* **124**, 204502 (2020), publisher: American Physical Society.
- [45] C. Rodda, C. Savaro, G. Davis, J. Reneuve, P. Augier, J. Sommeria, T. Valran, S. Viboud, and N. Mordant, Experimental observations of internal wave turbulence transition in a stratified fluid, *Physical Review Fluids* **7**, 094802 (2022), publisher: American Physical Society.
- [46] T. L. Reun, B. Favier, and M. L. Bars, Parametric instability and wave turbulence driven by tidal excitation of internal waves, *Journal of Fluid Mechanics* **840**, 498 (2018), publisher: Cambridge University Press.
- [47] R. Meyrand, S. Galtier, and K. H. Kiyani, Direct evidence of the transition from weak to strong magnetohydrodynamic turbulence, *Physical Review Letters* **116**, 105002 (2016), publisher: American Physical Society.
- [48] T. Le Reun, B. Favier, A. J. Barker, and M. Le Bars, Inertial wave turbulence driven by elliptical instability, *Physical Review Letters* **119**, 034502 (2017), publisher: American Physical Society.
- [49] T. L. Reun, B. Favier, and M. L. Bars, Experimental study of the nonlinear saturation of the elliptical instability: inertial wave turbulence versus geostrophic turbulence, *Journal of Fluid Mechanics* **879**, 296 (2019), publisher: Cambridge University Press.
- [50] M. Brunet, B. Gallet, and P.-P. Cortet, Shortcut to geostrophy in wave-driven rotating turbulence: The quartetic instability, *Physical Review Letters* **124**, 124501 (2020), publisher: American Physical Society.
- [51] E. Monsalve, M. Brunet, B. Gallet, and P.-P. Cortet, Quantitative experimental observation of weak inertial-wave turbulence, *Physical Review Letters* **125**, 254502 (2020), publisher: American Physical Society.
- [52] N. Lanchon, D. O. Mora, E. Monsalve, and P.-P. Cortet, Internal wave turbulence in a stratified fluid with and without eigenmodes of the experimental domain, *Phys. Rev. Fluids* **8**, 054802 (2023).
- [53] P. Müller, G. Holloway, F. Henyey, and N. Pomphrey, Nonlinear interactions among internal gravity waves, *Reviews of Geophysics* **24**, 493 (1986), eprint: <https://onlinelibrary.wiley.com/doi/pdf/10.1029/RG024i003p00493>.
- [54] Y. V. Lvov, K. L. Polzin, and N. Yokoyama, Resonant and near-resonant internal wave interactions, *Journal of Physical Oceanography* **42**, 669 (2012), publisher: American Meteorological Society Section: Journal of Physical Oceanography.
- [55] Y. V. Lvov, K. L. Polzin, E. G. Tabak, and N. Yokoyama, Oceanic internal-wave field: Theory of scale-invariant spectra, *Journal of Physical Oceanography* **40**, 2605 (2010), publisher: American Meteorological Society Section: Journal of Physical Oceanography.
- [56] C. H. McComas and F. P. Bretherton, Resonant interaction of oceanic internal waves, *Journal of Geophysical Research* (1896-1977) **82**, 1397 (1977), eprint: <https://onlinelibrary.wiley.com/doi/pdf/10.1029/JC082i009p01397>.
- [57] J. A. MacKinnon, M. H. Alford, O. Sun, R. Pinkel, Z. Zhao, and J. Klymak, Parametric subharmonic instability of the internal tide at 29°N, *Journal of Physical Oceanography* **43**, 17 (2013), publisher: American Meteorological Society Section: Journal of Physical Oceanography.
- [58] S. V. Nazarenko and A. A. Schekochihin, Critical balance in magnetohydrodynamic, rotating and stratified turbulence: towards a universal scaling conjecture, *Journal of Fluid Mechanics* **677**, 134 (2011), publisher: Cambridge University Press.
- [59] A. Craya, Contribution à l'analyse de la turbulence associée à des vitesses moyennes (1957).
- [60] Y. V. Lvov and N. Yokoyama, Nonlinear wave-wave interactions in stratified flows: Direct numerical simulations, *Physica D: Nonlinear Phenomena* **238**, 803 (2009).
- [61] A. V. Mohanan, C. Bonamy, M. C. Linares, and P. Augier, FluidSim: Modular, object-oriented python package for high-performance CFD simulations, *Journal of Open Research Software* **7**, 14 (2019), number: 1 Publisher: Ubiquity Press.
- [62] P. Augier, A. V. Mohanan, and C. Bonamy, FluidDyn: A python open-source framework for research and teaching in fluid dynamics by simulations, experiments and data processing, *Journal of Open Research Software* **7**, 10.5334/jors.237 (2019).
- [63] A. V. Mohanan, C. Bonamy, and P. Augier, FluidFFT: Common API (C++ and Python) for fast fourier transform HPC libraries, *Journal of Open Research Software* **7**, 10.5334/jors.238 (2019).
- [64] S. de Bruyn Kops and J. Riley, Direct numerical simulation of laboratory experiments in isotropic turbulence, *Physics of*

- Fluids **10**, 2125 (1998).
- [65] L. M. Smith and F. Waleffe, Generation of slow large scales in forced rotating stratified turbulence, *Journal of Fluid Mechanics* **451**, 145 (2002), publisher: Cambridge University Press.
- [66] J.-P. Laval, J. C. McWilliams, and B. Dubrulle, Forced stratified turbulence: Successive transitions with reynolds number, *Physical Review E* **68**, 036308 (2003), publisher: American Physical Society.
- [67] F. S. Godeferd, A. Delache, and C. Cambon, Toroidal/poloidal modes dynamics in anisotropic turbulence, in *Turbulence and Interactions*, Notes on Numerical Fluid Mechanics and Multidisciplinary Design, edited by M. Deville, T.-H. Lê, and P. Sagaut (Springer, 2010) pp. 151–158.
- [68] M. Nikurashin and S. Legg, A mechanism for local dissipation of internal tides generated at rough topography, *Journal of Physical Oceanography* **41**, 378 (2011).
- [69] P. Bartello, Geostrophic adjustment and inverse cascades in rotating stratified turbulence, *Journal of Atmospheric Sciences* **52**, 4410 (1995).
- [70] M. C. Linares, Numerical study of 2d stratified turbulence forced by internal gravity waves (2020).
- [71] S. S. Cerri, T. Passot, D. Laveder, P.-L. Sulem, and M. W. Kunz, Turbulent regimes in collisions of 3d alfvén-wave packets (2022), 2207.04301 [astro-ph, physics:physics].
- [72] C. Garrett and W. Munk, Internal waves in the ocean, *Annual Review of Fluid Mechanics* **11**, 339 (1979), eprint: <https://doi.org/10.1146/annurev.fl.11.010179.002011>.
- [73] C. Herbert, R. Marino, D. Rosenberg, and A. Pouquet, Waves and vortices in the inverse cascade regime of stratified turbulence with or without rotation, *Journal of Fluid Mechanics* **806**, 165 (2016), publisher: Cambridge University Press.
- [74] M. L. Waite, Potential enstrophy in stratified turbulence, *Journal of Fluid Mechanics* **722**, R4 (2013).